



Solar Mass Ejection Imager (SMEI) observations of coronal mass ejections (CMEs) in the heliosphere

D. F. Webb,¹ D. R. Mizuno,¹ A. Buffington,⁴ M. P. Cooke,⁵ C. J. Eyles,⁵ C. D. Fry,⁶ L. C. Gentile,¹ P. P. Hick,⁴ P. E. Holladay,² T. A. Howard,⁷ J. G. Hewitt,² B. V. Jackson,⁴ J. C. Johnston,² T. A. Kuchar,¹ J. B. Mozer,² S. Price,² R. R. Radick,³ G. M. Simnett,⁵ and S. J. Tappin⁵

Received 7 February 2006; revised 19 May 2006; accepted 12 July 2006; published 1 December 2006.

[1] The Solar Mass Ejection Imager (SMEI) on the Coriolis spacecraft has been obtaining white light images of nearly the full sky every 102 minutes for three years. We present statistical results of analysis of the SMEI observations of coronal mass ejections (CMEs) traveling through the inner heliosphere; 139 CMEs were observed during the first 1.5 years of operations. At least 30 of these CMEs were observed by SMEI to propagate out to 1 AU and beyond and were associated with major geomagnetic storms at Earth. Most of these were observed as frontside halo events by the SOHO LASCO coronagraphs.

Citation: Webb, D. F., et al. (2006), Solar Mass Ejection Imager (SMEI) observations of coronal mass ejections (CMEs) in the heliosphere, *J. Geophys. Res.*, *111*, A12101, doi:10.1029/2006JA011655.

1. Background

1.1. Introduction

[2] The Solar Mass Ejection Imager (SMEI) was launched on 6 January 2003 from Vandenberg Air Force Base into a Sun-synchronous polar orbit, one of two instruments on the Department of Defense Space Test Program's Coriolis satellite. Conceived as an all-sky imager [Jackson *et al.*, 1989], SMEI views the outward flow of density structures emanating from the Sun by observing Thomson-scattered sunlight from heliospheric plasma. These structures include solar coronal mass ejections (CMEs), corotating structures (streamers), and other solar wind density enhancements or depletions, such as variations behind shock waves. The primary objective of SMEI is to demonstrate the feasibility of using such instrumentation to forecast the arrival of the CMEs at Earth. The SMEI instrument may be regarded as a successor to the zodiacal light photometers [Leinert *et al.*, 1975] on the twin Helios spacecraft; it exploits the heliospheric remote sensing capability dem-

onstrated by that instrument [Jackson, 1985; Webb and Jackson, 1990].

[3] Jackson *et al.* [2004] provide the history of the SMEI design and development, including a description of the mission, data handling and removal of background sources during image processing. The instrument design, architecture, testing and qualification procedures are described by Eyles *et al.* [2003]. Webb *et al.* [2002] discuss the motivation for SMEI as a proof-of-principle experiment for a new kind of space weather forecasting tool.

1.2. SMEI Design, Operations, and Ground Processing

[4] SMEI was designed to observe and obtain time sequences of heliospheric phenomena propagating from the Sun through interplanetary space. It achieves this by imaging nearly all the sky every 102 minutes, the spacecraft's orbital period, with sufficient sensitivity and photometric stability to be able to detect faint transient disturbances against the much brighter, but relatively unchanging stellar and zodiacal background. SMEI has achieved its primary objective, observing 139 CMEs during the first 1.5 years of operations and more than 200 CMEs to date. SMEI also has demonstrated the potential ability to detect Earth-directed CMEs well in advance of their arrival [Tappin *et al.*, 2004; Howard *et al.*, 2006].

[5] The Coriolis satellite is in a dawn-dusk, Sun-synchronous, circular polar orbit at an altitude of 840 km. and an inclination of 98° relative to the equatorial plane. The SMEI sensor suite consists of three carefully baffled CCD (charge-coupled detector) cameras, each covering a narrow 3° × 60° strip of the sky. The cameras are mounted on the satellite with their fields of view (FOV) aligned end-to-end and slightly overlapping, so that the FOV swath is a 3° wide strip extending 160° along an approximate great circle with the ends near the orbit axis. Figure 1a is a schematic of the

¹Institute for Scientific Research, Boston College, Chestnut Hill, Massachusetts, USA.

²Air Force Research Laboratory, Space Vehicles Directorate, Hanscom Air Force Base, Massachusetts, USA.

³Air Force Research Laboratory, Space Vehicles Directorate, Sunspot, New Mexico, USA.

⁴Center for Astrophysics and Space Sciences (CASS), University of California, San Diego, La Jolla, California, USA.

⁵School of Physics and Astronomy, University of Birmingham, Birmingham, UK.

⁶Exploration Physics International, Incorporated, Huntsville, Alabama, USA.

⁷Physics Department, Montana State University, Bozeman, Montana, USA.

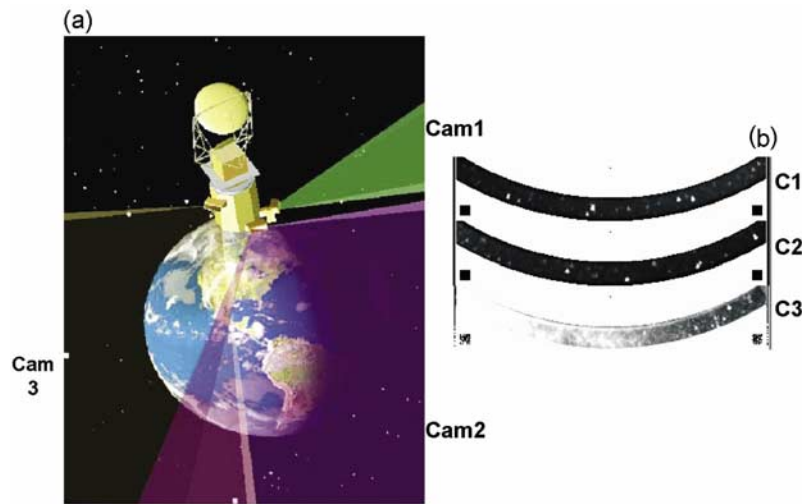


Figure 1. (a) Schematic of SMEI on the Coriolis spacecraft. Spacecraft orbit is nearly circular at 840 km above Earth. The three SMEI cameras view outward from Earth and together their FOV cover an $\sim 160^\circ$ swath of the sky directed $\sim 30^\circ$ above the local horizontal to avoid light from the Earth and sunlight reflecting from the rotating Windsat antenna. (b) Individual 4-s exposure frames, covering $3^\circ \times 60^\circ$, from each of the three cameras. From top to bottom: Camera 1 viewing the antisolar night sky, Camera 2 toward the zenith over the terminator, and Camera 3 closest to the Sun.

satellite in orbit, showing the FOV of the three cameras, which are mounted on the lower, three-axis stabilized platform, and Figure 1b shows the individual $3^\circ \times 60^\circ$ data frame images from each camera. Since the satellite has zenith-nadir pointing, the cameras' FOV sweep out nearly 90% of the entire sky during each orbit. Gaps in coverage include a zone of exclusion of $\sim 20^\circ$ radius centered on the approximate sunward orbital pole, a smaller circle in the opposite direction, and occasional areas shuttered because of sunlight in the sunward camera. The instrument operates continuously, so the primary data product comprises a sequence of 14 orbits of images per day. It has maintained a duty cycle of 85% interrupted only for periodic calibration and diagnostic purposes and occasional software anomalies and telemetry problems. The cameras' unfiltered

CCDs have a red-biased spectral response from ~ 400 to 1100 nm that peaks at 700 nm.

[6] Individual $3^\circ \times 60^\circ$ data frames (Figure 1b) are combined to form composite heliospheric all-sky maps. The choice of the coordinate system for representing the entire celestial sphere projected in two dimensions involves a trade-off between simplicity of interpretation on one hand and minimal distortion on the other. The Sun-centered, equal area Hammer-Aitoff projection [e.g., Leighly, 1955] selected for the orbit maps discussed here provides a reasonably undistorted representation of the sunward hemisphere, where most heliospheric disturbances are best observed, but at the cost of more serious distortion around the perimeter of the image region, corresponding to the poles and the antisunward meridian. In a Hammer-Aitoff projection of the whole

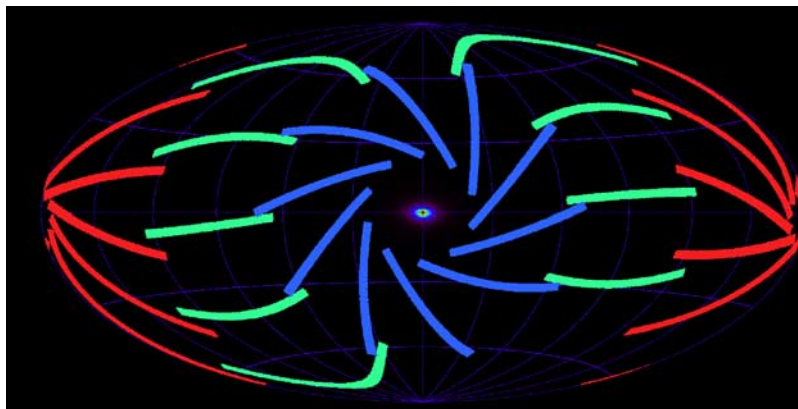


Figure 2. Example showing how individual $3^\circ \times 60^\circ$ data frames (Figure 1b) are combined in a composite heliospheric sky map. Representative camera frames for one orbit are shown as they are mapped in ecliptic coordinates onto a Hammer-Aitoff, equal area projection map with a nominal pixel size of 0.5° and a resolution of $\sim 1^\circ$. Colors refer to a given camera: 3 = blue, 2 = green, 1 = red. About 1500 frames from each camera are used to form an orbital map.

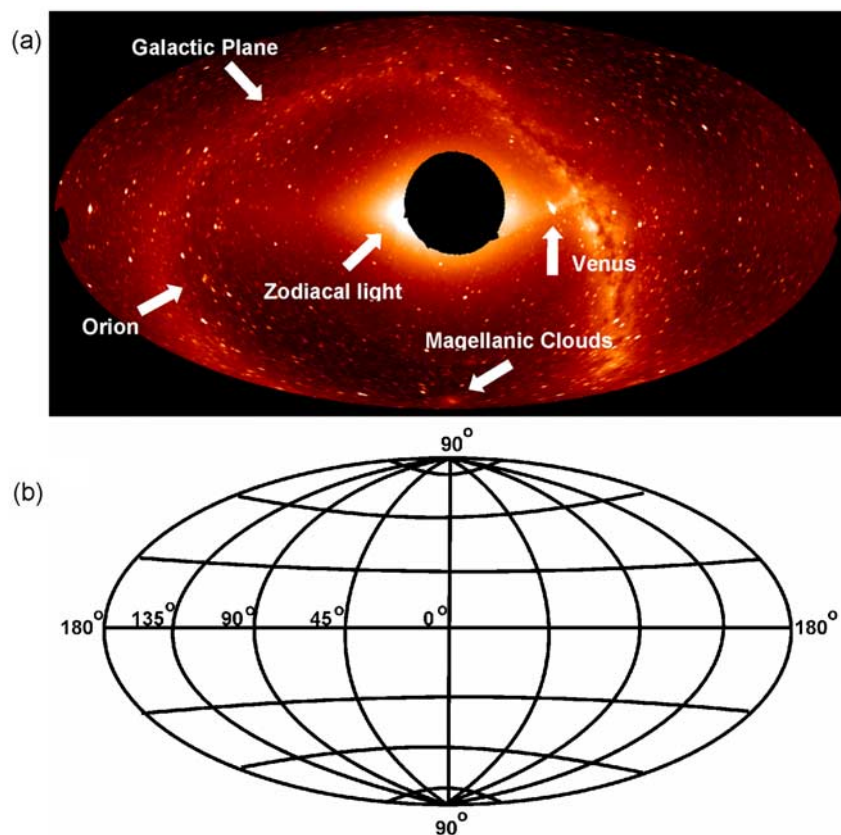


Figure 3. (a) SMEI image of the entire sky. A full orbit of frames are registered onto a high-resolution sky map to build a composite view that can be projected as a full-sky Hammer-Aitoff map. This image is a composite of frames from several orbits on 18 February 2003 with various bright features labeled. (b) Hammer-Aitoff projection Sun-centered, ecliptic coordinate system; The ecliptic plane is the central horizontal line, the upper and lower 90° points are the north and south ecliptic poles, respectively, and the antisolar direction is at the 180° point.

sky, the surface area of the celestial sphere is preserved on a two-dimensional representation of the image. Figure 2 shows how this “stitching” is done for a full map. A “first light” example of such a map is shown in Figure 3a. The Sun is centered in these equal area projections, with ecliptic north at the top and east to the left (Figure 3b).

[7] Like any white light coronagraph, SMEI, is designed to measure heliospheric Thomson-scattered light integrated along each line of sight. However, the brightness of this emission falls off exponentially or greater with distance from the Sun. Therefore special care is needed in generating the full-sky SMEI images to insure that the variations in brightness from these very faint signals are detectable over the entire sky. The integration time for each CCD camera frame is 4 sec. The raw frames for two cameras are averaged over 4×4 pixel bins on board the spacecraft before transmission to the ground, while 2×2 binning is used for the third, sunward camera because of the thermal effects of that camera (see below). On the ground, the CCD frames are processed and assembled into the all-sky orbit images. For each frame, the dark offset and electronic bias are subtracted, and other conditioning is performed as described by Mizuno *et al.* [2005] and Jackson *et al.* [2004]. The processed frames are position tagged, registered and averaged together on a standard grid in fixed sidereal coordinates

at approximately the same spatial sampling, ~ 12 arc-min, as in the original CCD frames. The pixels in this intermediate representation are then resampled onto the Sun-centered Hammer-Aitoff projection in ecliptic coordinates, at the lower spatial resolution.

[8] The light baffles were designed to meet the SMEI photometric specification, provided the solar limb does not approach the camera axis within 18° and 57° in the cameras’ narrow and wide dimensions, respectively [Buffington *et al.*, 2003]. When a SMEI camera points close to the Sun, sunlight illuminates inner portions of the baffle and, as discovered on orbit, is sufficiently bright to saturate the CCD with a 4-sec exposure. The sunward edge of the Camera 3 FOV is offset 20° from the sunward pole of the orbital plane creating a circular zone of avoidance $\sim 20^\circ$ in radius on the orbit maps. However, the pole of the orbital plane is at a declination of about -10° , so the Sun travels outside this exclusion zone reaching its farthest limits during the solstices. To protect the CCD, a shutter in the light path closes when the solar illumination is too high. The baffle also rejects background light other than the Sun, including illuminated spacecraft appendages and instrumentation, as well as Earthshine. All of the SMEI cameras are arranged on Coriolis so that they point away from the Earth to minimize Earthshine, and

away from the rotating antenna of the other experiment, Windsat (Figure 1a).

1.3. Background Light Sources, Instrumental Effects, and Heliospheric Map Production

[9] All 3 CCD camera systems were intended to operate at -30°C to minimize noise and on-orbit radiation effects over the nominal mission lifetime of 3 years. Despite some variation caused by seasonal effects in this Sun-synchronous orbit, Cameras 1 and 2 do operate around this temperature. However, the sunward Camera 3 operates between -2 and -15°C , at much higher temperatures than intended (see *Eyles et al.* [2003], section 3.7, for a discussion). The higher operating temperature lowers the overall sensitivity in Camera 3 and efforts are being made to mitigate these effects. This higher temperature raises the average dark current, which in turn introduces significant noise to each individual pixel readout. In addition, a population of “hot pixels” appears, which increases with time because of particle-induced radiation damage on the CCD. This latter effect is partially remedied by periodic annealing (heating) of the CCD. Eventually specialized ground processing of the Camera 3 frames may be able to eliminate much of this radiation-induced noise, but it remains in the sky maps used in the CME analysis results discussed here.

[10] Because the SMEI data have only a preliminary calibration [e.g., *Jackson et al.*, 2004, 2005; 2006], the brightness values in this study are not in terms of physical units, but the analog-to-digital units, ADUs, of the transmitted CCD frames. For reference, the Galactic plane has a typical surface brightness of ~ 200 ADU, with peak brightness near the Galactic center of ~ 1000 ADU, while the zodiacal light is much brighter nearer the Sun. In comparison, CMEs have peak brightnesses of only $\sim 1-6$ ADU, confirming premission estimates that their detectability in the heliosphere is at 1% of the background [see *Jackson et al.*, 2004]. After all corrections are applied, the ADU scale is proportional to the integrated band radiance as measured by the SMEI instrument. *Mizuno et al.* [2005] obtained a preliminary estimate for the conversion factor to be $1 \text{ ADU} = 36 \text{ Rayleighs}$ ($1 \text{ Rayleigh} = 10^{10}/4\pi \text{ photons s}^{-1} \text{ m}^{-2} \text{ sr}^{-1}$) with an uncertainty of $\sim 3\%$. Astronomers use other units for surface brightness, such as S10, the brightness equivalent to the flux of a tenth magnitude solar-type star per square deg. of sky. Two preliminary studies suggest that one S10 is approximately 0.55 SMEI ADUs [*Buffington et al.*, 2004] or 0.4 ADUs [*Buffington et al.*, 2006].

[11] The cameras scan the sky across their narrow dimension and a given point on the sky transits this 3° field in about a minute; the transit time varies as the inverse of the cosine of the angle from the orbital plane. A given point in the final all-sky images is an average of many input values accumulated over 10 or more CCD frames. The typical total RMS noise in a single input frame in the lowest background regions is ~ 1.0 ADU, which is reduced by a factor of 10 in the composite all-sky images [*Mizuno et al.*, 2005; *Buffington et al.*, 2006, Figure 6]. Thus with current processing SMEI has a sensitivity that is sufficient to detect objects with surface brightnesses less than 1 ADU.

[12] The background due to individual stars, the extended emission from the Galactic plane, and zodiacal light are each far brighter than the faint heliospheric structures that

SMEI is designed to detect. An advanced technique being developed at UCSD to remove these background signals and the initial results for the Halloween, 2003 storm period are described by *Jackson et al.* [2006] and summarized in section 3. However, the production pipeline used in the present analysis removes, or reduces, these backgrounds by taking the difference between the image for the current orbit and the image for either the immediately preceding orbit or the average of several preceding orbits. Such subtractions are called “running differences” and have been successfully used to detect subtle transients in SOHO EIT (Extreme ultraviolet Imaging Telescope: *Delaboudiniere et al.* [1995]) and LASCO (Large Angle and Spectrometric Coronagraph: *Brueckner et al.* [1995]) movies. We call these orbit difference image maps “near real time difference” or NRTD maps. This technique has the advantage of providing efficient removal of the main background signals and fixed instrumental artifacts, but requires that the target objects move or change significantly from orbit to orbit. In effect, a constant heliospheric signal cancels out in the difference map, leaving only the *changes* in heliospheric structures from one orbit to the next. We have found that CMEs and other heliospheric features are too faint to be detectable on direct orbit maps or movies made from them, but become readily observable as moving structures on movies of the NRTD maps. Thus the CMEs have been identified, tracked and their characteristics measured interactively from the NRTD movies. This procedure does remove some of the true surface brightness of a CME; therefore the CME brightnesses measured from orbit differences and given in Table 1 are lower limits.

[13] The direct and differenced orbital images still contain features and artifacts including the residuals from bright stars, data dropouts, and saturated regions due to the Moon, bright planets, and proximity to the Sun. Another artifact that is caused by the interactions of trapped radiation belt particles with the CCD and its processing electronics occurs on nearly every orbit and can affect large numbers of CCD pixels. These particles typically appear as the satellite crosses the polar auroral zones and during passages through the South Atlantic Anomaly (SAA). In the auroral zones the particles are most likely electrons that are collimated by the baffles and scatter off the first mirror (M1). In the SAA high-energy protons either pass directly through the optics detector chamber walls or produce byproducts [*Eyles et al.*, 2003; *Buffington et al.*, 2005]. On the orbital maps these regions appear as large-area bands in which all the cameras simultaneously have a very granular appearance in the difference images. On the original CCD frames these particle interactions are manifested as a random scattering of data bins with elevated values that render large and variable areas of the maps unusable for CME detection. Although a spike removal algorithm is routinely applied in the current map processing, particle spike “dropouts” remain a significant problem with the NRTD technique.

[14] Another “artifact” is an occasional visible light phenomenon that we associate with the geo-aurora [*Mizuno et al.*, 2005]. This phenomenon is localized to the auroral zones and polar regions and typically appears in a single isolated orbit. SMEI’s observations of the aurora at this high altitude (>840 km) were unanticipated and constitute a major discovery. Auroral brightnesses measured by SMEI

vary from a few to several hundred ADUs, and are well correlated in both brightness and frequency with periods of enhanced geomagnetic activity, i.e., when the indices Kp and Dst have peak values >6 and <-60 nT, respectively [Mizuno *et al.*, 2005].

[15] Finally, the Moon, which follows a predictable path on the ecliptic projection maps, is always moving through the all-sky view and, when bright enough, saturates several adjacent frames from a given camera. The bright planets also traverse the all-sky view but affect only a few adjacent sky map bins per orbit. Jupiter, the largest planet, affects ~ 30 bins.

[16] Figure 4 illustrates these artifacts (except for the Moon) along with a true CME on a difference image. The open arrows point to missing data due to the exclusion zone, shuttered frames due to bright sunlight, particle enhancements from the polar zones and SAA, and auroral light. The CME (shaded arrows) consists of faint arcs seen in three unobscured areas of the inner heliosphere.

2. SMEI Observations of CMES

[17] Since early February 2003, SMEI has taken data in its nominal observation mode with a duty cycle of 85%. Using the full-sky heliospheric NRTD maps, 139 CMES were detected during the first 1.5 years of operations. About 30 of these SMEI CMES were likely directed Earthward, and most were first manifest as “halo” CMES near the Sun with associated frontside surface activity as seen by the SOHO LASCO coronagraphs [Brueckner *et al.*, 1995]. We next discuss details of the SMEI observations of CMES.

2.1. CME Search Criteria and Data Products

[18] We searched the all-sky, Hammer-Aitoff maps for large-scale, transient structures that might be associated with density manifestations of CMES traversing the inner heliosphere. Nearly all of these transients were initially identified by one of us (D. Mizuno) in a systematic interactive survey using the orbital NRTD maps viewed as movies on a computer monitor. To be identified as a CME, a structure had to be moving approximately radially outward from the Sun and be broad enough both in angular span and radial extent to preclude its being an artifact. The outward motion had to persist over five or more consecutive orbits (four if the structure entered a particle contamination zone or other region of obscuration). If several components were observed at approximately the same time and position angle, they were listed as a single CME unless there was an obvious difference in angular speed. In that case they were listed as separate CMES.

[19] Table 1 (see explanation in next section) presents basic information and measurements for the SMEI CMES through the first 1.5 years. Peak brightness and angular span were usually measured from the earliest orbit image on which the CME was detected, unless it was partially obscured (usually by particles). In that case a later, less obscured image provided the span. The brightness is an average in ADU of a typical point on the CME and is only an estimate, accurate to about ± 0.5 ADU. Even on these NRTD maps, the CMES are just above a minimum brightness detection threshold.

[20] The distance from the Sun traversed by a CME is typically characterized by its solar elongation angle ε . In ecliptic coordinates, the center of the Sun is at $\varepsilon = 0^\circ$, ε is the polar distance, and position angle (PA) is the associated polar coordinate. Coronal structures viewed via Thomson scattering with traditional coronagraphs are projections onto the “plane of the sky” which, near the Sun, is the plane orthogonal to the line of sight containing the Sun. For a given ε this assumption fixes an approximate distance in km or solar radii above the solar limb and enables plotting the trajectory of a CME structure on a height versus time plot. As material moves farther and farther out from the Sun, its relationship to this plane of the sky becomes more indeterminate.

[21] For SMEI, the elongation ε of the CME on a given map is the basic measurement and thus ε versus time plots provide the primary information on the outward motion of the CME. The approximate PA of the center of the CME is determined, and the ε of that point is measured on all NRTD maps on which the CME can be followed. The PAs are measured with respect to the ecliptic north pole, counter-clockwise to the east. (The PAs measured in a coronagraph are determined with respect to the *solar* north pole and, thus can differ by up to 7° during the year.) An ε value is measured from the transition between the leading bright component and the trailing shadow in the difference map, and thus trails the “true” leading edge of the CME by an amount that depends on the speed of the CME over several orbits.

[22] The initial coordinates are measured in terms of bins on the NRTD sky map, and then converted to sidereal and Sun-centered (ecliptic) coordinates. Each orbital map for a given camera has an initial starting location and time. Then, for a given bin, the observation time is estimated by evolving the spacecraft pointing coordinates until that corresponding coordinate crosses the centerline of the camera. The resulting time measurements are actually uncertain by an amount that depends approximately on the angular span of the CME.

[23] Once a possible CME was cataloged, special NRTD maps were produced with an appropriate contrast/brightness “stretch” for that particular event. These event images and the measured ε time plots were then saved and the images were made into movies. The movies and the ε -time plots were then evaluated independently by other team members to confirm each event.

[24] In summary, each of the CMES detected from the SMEI NRTD maps has (1) NRTD images and distance-time data and plots, (2) movies made from these images, (3) a file of comments, (4) preliminary “CME Search List” containing SMEI and LASCO operational information and lists of SMEI CMES and candidate associated LASCO CMES, and (5) a catalog of the basic measured data for each listed CME.

2.2. Statistical Results

[25] Data for each CME were compiled in a “SMEI CME Summary List”, a reduced version of which appears here as Table 1 with 12 columns as follows: (1) Year and Day of Year (DOY) when CME first observed, (2) Equivalent date (day-month), (3) Degree of certainty of CME identification/Quality of observation, (4) Time when CME first observed (UT), (5) Duration of observation (hours), (6) Position angle/location of CME axis (degrees/direction), (7) Angular span of CME (degrees), (8) Brightness of CME (ADUs),

Table 1. Catalog of CMEs Observed by SMEI

Year, DOY	Date	Conf ^a	First Obs. Time, UT ^b	Duration, hours	Position Angle/ Location, deg./dir ^c	Angular Span, deg	Peak Brightness, adu	Type	Angular Speed, deg/hour	Point P Speed, km/sec	Elongation Range, deg ^d
2003											
41	10 Feb	P	12:32	10	44.3/NE	23.4	1.0	2 arcs	0.38	232	30.2–33.9
42	11 Feb		21:10		.../SE			arcs			
43	12 Feb	P	16:15	12	231/SW	20.3	0.5	arc	0.52	339	23.0–28.9
44	13 Feb	P	8:24	8.50	30/NNE	16.3	2.0	blob			38.6–36.0
45	14 Feb	P	2:41	14	105/ESE	23.3	1.0	arc	0.77	494	22.6–32.3
47	16 Feb	G	10:36	13.5	96/E	75.1	0.5	loop(s)	0.44	283	23.4–29.7
48	17 Feb	P	12:54	8	280/WNW	23.3	0.5	arc	0.46	288	28.7–32.6
50	19 Feb	V	5:12	12	330/NW	44.4	1.0	loop/arc	1.00	602	27.8–39.8
52	21 Feb	V	2:00	44	358; 19	16; 29	1.0;1.0	several arcs	0.72;0.76	394;414	27.0–49.7
54	23 Feb	P	6:38	8.5	157/SSE	50.0	0.5	loop	0.59	379	25.0–30.1
55	24 Feb	G	4:42	35	145;143	18; 25	2.0;2.0	2 arcs	0.49;0.56	314;348	20.5–33.7
55	24 Feb	?	12:48								
58	27 Feb	P	17:11 (JT)		.../SSE			arcs			
60	1 Mar	G	19:12	13	329/NW	10.3	2.0	blob	0.40	254	26.2–31.3
60	1 Mar	E	21:53	25	130/SE	62.6	1.0	loops	0.76	450	24.7–45.0
62	3 Mar	G	6:04	7	125/SE	62.6	1.0	arc	0.56	354	26.1–29.7
63	4 Mar	P	2:08	17.5	112/ESE	13.5	0.5	arc	0.34	200	31.8–37.9
63	4 Mar	G	16:10	29	85/E	97.0	0.5–1.0	loop	0.77;1.05	462;682	21.8–44.2
66	7 Mar	P	14:06	10	335/NW	5.4	0.5	blob	0.47	300	26.2–31.0
71	12 Mar	P	8:54	7	44/NE	4.9	0.5	blob	0.55	374	19.2–22.8
72	13 Mar	P	0:27		NNE			arcs			
72	13 Mar	V	10:24	21	20/NNE	20.1	1.5	V arc	0.60	397	16.7–28.7
72	13 Mar	P	20:29	7	53/ENE	31.3	0.5	arcs	1.32	855	21.2–30.2
77	18 Mar	?	2:18	12	8/NNE	11.2	0.5	?	0.73	444	28.4–37.2
78	19 Mar	G	19:01	20	336/NW	54.4	0.5	arc	0.67	425	21.8–34.1
81	22 Mar	P	23:16	24	350/N	44.6	0.5	arc-loop	0.65;0.86	430;526	21.6–42.3
83	24 Mar	P	12:39	8.5	1/N	59.5	0.5	loop	1.08	610	34.3–43.8
85	26 Mar	G	13:33	13.5	341/NNW	44.7	1.0	2 arcs	0.65	428	19.9–28.7
86	27 Mar	P	18:20	6.5	342/NNW	9.6	1.0	arc	0.66	432	22.8–27.5
96	6 Apr	G	17:20	8+	293/NNW	21.3	0.5	arc	0.55–0.58	362–374	25.0–29.9
97	7 Apr	V	16:40	12	71/ENE	53.2	1.0	arc	0.93	100	75.5–86.8
108	18 Apr	G	0:05	25	15/NNE	27.8	0.6	arc	0.61	197	55.1–70.7
110	20 Apr	V	11:21	30.5	13/NNE	35.4	0.3	2 arcs	0.76;1.37	128;299	51.1–91.9
115	25 Apr	V	5:02	20	330/NW	49.8	1.0	V arc	1.06	621	25.7–47.1
116	26 Apr	P	13:07	15.5	311/NW	10.4	0.3	blob	0.54	337	26.5–34.7
118	28 Apr	P	9:08	8.5	290/WNW	37.9	1.0	arc	0.73	481	21.3–28.0
119	29 Apr	G	6:59	3.5	38/NE	21.8	0.3	2 loops	0.89	391	50.8–53.8
123	3 May	V	2:33	36	358/N	23.4	0.2	arcs	0.60	194	53.2–72.5
125	5 May	V	8:39	24	25;26;342 NE-NW	30; 20; 30.0	1.0	arcs	0.65;0.79 1.05	291;334 434	43.9–64.6
133	13 May	V	4:36	48	17/NNE	48.0	1.0	arcs	0.64	301	37.8–60.2
140	20 May	G	19:32	15	4/N	17.1	1.0	2 arcs	1.03	504	39.2–55.0
148	28 May	E	16:53	24	284/WNW	89.1	0.5	halo	1.76	758	32.4–74.8
150	30 May	G	18:18	27	355/N	25.0	0.3	arc	0.69	324	39.0–60.2
151	31 May	E	16:31	8.5	248/WSW	61.9	1.0	loop	1.99	1164	27.5–43.9
153	2 Jun	G	15:56	11	240/SW	47.1	1.0	loop	1.32	778	28.3–41.8
154	3 Jun	G	20:31	24;22	13; 350	54.2	0.5	loop	0.85;0.45	432;216	35.4–54.6
159	8 Jun	P	22:26	11.5	9/N	22.3	0.5	arc	0.70	324	46.3–54.5
164	13 Jun	E	0:45	3.5	305/NW	39.9	5.0	loop	1.12	715	26.1–29.9
165	14 Jun	V	10:36	39	325;319	36.6	0.5	arcs	0.94;1.16	489;562	26.2–72.9
175	24 Jun	G	11:10	10	260/WSW	73.4	1.0	loop	1.30	804	24.5–38.0
175	24 Jun	P	22:43	7	31/NNE	15.6	1.5	arc	0.53	306	34.4–37.8
177	26 Jun	E	12:04	32	354/N	24.0	0.5	arcs	1.23	456	38.3–77.5
186	5 Jul	G	6:05	27	345/NNW	23.3	0.2	arc	0.53	182	54.5–68.8
191	10 Jul	E	6:16	25.5	357/N	30.2	0.5	arc	0.94	411	40.7–64.1
		E	4:43	27	310/WNW	48.1	0.7	arc	0.65	372	28.7–47.0
193	12 Jul	G	14:15	8.5	332/242	25;15	0.5	arc	0.91;0.59	518;378	24.9–42.0
200	19 Jul	P	20:35	12	351/N	19.2	0.5	arc	1.14	520	44.3–57.7
204	23 Jul	G	2:32	5	323/NW	54.0	0.5	arc	1.43	792	36.2–43.5
205	24 Jul	V	20:44	12	00/N	19.1	0.5	arc	1.08	336	58.2–70.6
205	24 Jul	P	20:57	10	298/WNW	37.9	1.0	arc	0.80	505	25.4–33.5
206	25 Jul	E	17:14	2+d.	305/NW	47;40	1.0	V arc	0.91–1.02	437–336	25.5–71.9
206	25 Jul	E	23:53	10	6.5/N	73.8		arc	3.38	1222	42.0–78.1
207	26 Jul	E	6:37	10	88/E	73.8		arc	1.80	—	110–129
207	26 Jul	E	17:01	22.5	290;231	85;33	0.4	arc	4.89;3.42	123; —	61.8–121
210	29 Jul	V	5:48	15	350/NNW	32.5	0.5	2 arcs	1.23	567	40.7–59.8
214	2 Aug	P	10:17	24	330/NW	19.0	0.3	arc	0.56	237	47.4–60.9
217	5 Aug	P	7:13	13.5	324/NW	23.8	0.3	arc	0.59	256	48.8–57.5
218	6 Aug	V	18:45	8.5	330/NW	36.6	0.4	arc	1.02	452	47.9–56.5
219	7 Aug	?	2:02		.../NW			loops			

Table 1. (continued)

Year, DOY	Date	Conf ^a	First Obs. Time, UT ^b	Duration, hours	Position Angle/ Location, deg./dir ^c	Angular Span, deg	Peak Brightness, adu	Type	Angular Speed, deg/hour	Point P Speed, km/sec	Elongation Range, deg ^d
229	17 Aug	P	5:04	5	52/NE	18.1	0.3	arc	0.82	331	54.0–58.2
232	20 Aug	P	19:54	8.5	268/W	72.8(?)	0.3	loop	1.08	632	31.4–40.5
233	21 Aug	P	11:03	9.5	294/NW	23.6	1.0	arc	0.67	433	23.5–29.2
240	28 Aug	G	20:44	24	340/NNW	37.0	0.5	arc	0.71	271	48.6–65.7
245	2 Sep	P	5:53	10	269/W	58.1	0.5	2 loops	0.73	465	23.8–31.3
251	8 Sep	G	10:51	7	252/SW	43.7	0.5	loops	1.00	655	21.9–28.8
260	17 Sep	G	9:59	13.5	268/W	67.2	0.5	loop	0.48	313	20.8–28.3
264	21 Sep	P	0:41	5	276/W	55.8	0.0?	loop	0.77	518	18.9–22.9
293	20 Oct	P	4:30	10	108/ESE	10.5		arc	0.71	430	29.1–36.4
296	23 Oct	G	11:37	7	328;190	28;31	1.0;2.0	2 arcs	1.15;1.14	668;704	27.4–40.4
297	24 Oct	V	4:33	13.5	326;332	22.3	1.0	2 arcs	0.95;0.88	537;483	32.0–45.0
297	24 Oct	V	6:52	10	101/ESE	107.3	0.5	arc	3.37	51	70.8–106
297	24 Oct	V	16:08	7	294/NW	78.9	0.5	arc	4.22	—	82.4–112
300	27 Oct	V	6:49	15.5	275/W	95.4	6.0	loops	1.13	703	22.4–37.8
301	28 Oct	V	13:03	7; 6	297;115	37.1	1.0	2 arcs	2.57;1.86	1611;1054	21.0–44.7
304	31 Oct	P	5:27	3+	324/NW	28.5	1.0	arc	1.71	856	43.3–49.1
306	2 Nov	V	21:54	8.5	267/W	50.9	2.0	loop	2.04	1322	19.3–32.8
307	3 Nov	V	8:04	13.5	300/NW	50.9	2.0	loop	0.88	540	25.1–37.7
307	3 Nov	G	<13:09	3+	.../S			loop			
311	7 Nov	G	4:17	21	142;89	43;28	0.5	2 arcs	3.31;1.27	279;172	68.8–91.5
318	14 Nov	G	5:11	7	129/SE	23.0	1.0	arc	1.31	836	22.9–31.9
323	19 Nov	E	5:48	10	150/SSE	33.5	0.5	arcs	2.34	775	50.0–73.5
325	21 Nov	V	0:17	5+	111/SE	61.9	1.0	arc?	14.8?	—	65.5–142
325	21 Nov	G	4:19	7	324/NW	26.3	1.0	arc	1.01	615	29.1–35.9
334	30 Nov	V	2:36	12	135/SE	54.7	5.0	arc	0.68	433	23.2–31.3
No events in December											
2004											
1	1 Jan	P	6:40	29	141/SE	20.0	0.5	arc	0.71	324	39.2–60.3
3	3 Jan	V	6:04	17	92/ESE	70.5	1.0	loop	1.19	714	23.4–43.0
6	6 Jan	V	0:23	7	117/ESE	34.8	1.0	loop	1.92	1094	31.1–44.3
11	11 Jan	P	9:06	8.5	122/SE	35.8	0.5	arc	2.50	188	73.3–94.4
14	14 Jan	G	8:11	8.5	115/ESE	30.0	0.5	blob	0.77	508	21.0–27.6
21	21 Jan	V	3:48	9	133/SE	60.0	0.5	arcs	0.71	400	35.0–42.7
			22, 04:14	13.5	119/ESE	24.6	0.5	arc	0.98	180	67.8–81.4
22	22 Jan	G	3:31	12	115/ESE	60.0	1.0	loop	1.26	793	21.7–36.7
23	23 Jan	P	3:11	5.5	133/SE	7.5	1.0	blob	0.81	509	27.2–31.7
25	25 Jan	G	8:18	11	145/SSE	22.0	1.0	arc	0.72	459	24.6–33.0
38	7 Feb	P	20:10	10	58/NE	10.3	0.5	arc	0.77	379	43.3–50.9
40	9 Feb	G	20:54	~36	21–32	40;51	0.5	arc	1.25	—	42.1–102
47	16 Feb	E	7:01	17	114/ESE	81.5	2.0	loops	0.63	401	21.9–33.0
52	21 Feb	G	8:32	7	197/SSW	38.4	1.0	loop	1.10	717	21.7–29.3
53	22 Feb	P	23:38		.../SE						
68	8 Mar	E	16:42	3 d	NNW/ESE	65;25	1; 2	arcs	0.98	377	19.8–93.3
70	10 Mar	G	19:32	10	340/NW	35.3	1.0	arc	0.70	457	22.0–29.0
78	18 Mar	P	9:32		.../NW						
86	26 Mar	?	18:06	14	4/NE	44.0	0.5	loop	0.61	370	28.6–37.0
89	29 Mar	P	10:41	12	326/NW	10.7	1.0	blob	0.68	427	25.5–34.1
91	31 Mar	G	10:00	12.5	3/NNW	49.0	1.0	loop	0.71	447	25.0–33.8
92	1 Apr	G	9:42	?	N-NW	85;38	1; 0.5	loop			23.4–81.1
94	3 Apr	G	22:36	10	20/NE	54.8	0.5	arc	2.56	391	64.5–91.3
95	4 Apr	G	7:08	20	357/NNW	60.0	1.0	arc	0.76	443	28.3–43.8
95	4 Apr	G	18:56	12	44/NE	49.8	0.5	arc	1.19	142	73.4–87.8
101	10 Apr	P	19:43		.../NE						
105	14 Apr	P	0:45	10	25/NE	33.5	0.5	arc	1.06	355	57.0–67.5
117	26 Apr	?	14:31	10	275/W	3.3	1.0	blob	0.47	234	43.8–48.3
118	27 Apr	?	21:30		.../NE						
122	1 May	P	5:43	18	15/NE	30.1	1.0	arc	0.89	343	48.8–66.5
125	4 May	G	21:08	2.5d	.../SE			arc			
131	10 May	P	2:26	~27	23/NE	46.2	0.5	loops	0.66	241	50.4–69.6
143	22 May	G	13:22	24	356/N	86.5	0.5	loop	0.92	425	44.5–55.5
144	23 May		10:28		.../NNW						
145	24 May	P	0:55	12	354/N	~60		arc	0.93	380	49.0–61.5
148	27 May		19:27		.../NNE			blob			
149	28 May	V	6:29	27	13/NE	47.6	1.0	V arc	0.82	295	46.5–72.1
150	28 May	G	4:30	24	6–10/N	34.8	1.0	arc	0.98	431	40.7–65.3
175	23 Jun	G	9:08	10	306/WNW	51.3	2.0	loop	0.99	625	23.3–33.7
181	29 Jun	P	5:40	~12	290/NW	19.3	1.0	loop	0.76	488	24.3–30.0
192	10 Jul	V	7:34	35	292–306/NW	48;35	1; 1	loop	1.18	576	25.6–68.8
197	15 Jul	V	19:28	1.5d	330–341/NW	30;11.5	0.3,0.5	loops	0.77	350	35.7–60.4
202	20 Jul	G	21:28	5	278/WNW	25.1	1.0	arc	0.70	464	20.9–24.5

Table 1. (continued)

Year, DOY	Date	Conf ^a	First Obs. Time, UT ^b	Duration, hours	Position Angle/ Location, deg./dir ^c	Angular Span, deg	Peak Brightness, adu	Type	Angular Speed, deg/hour	Point P Speed, km/sec	Elongation Range, deg ^d
203	21 Jul	E	16:02	20	348;302	113;110	0.5; 1	loop	1.57;1.24	728;715	29.7–62.0
211	29 Jul	G	3:38	17	245/SW	39.9	1.0	loop	0.77	483	22.2–35.8

^aConfidence in CME identification or quality of event: E(xcellent), V(ery Good), G(ood), P(oor), ?(? Event).

^bSMEI orbital time as estimated at the position angle of the event.

^cPosition angle is the angle in degrees measured counterclockwise from ecliptic north through east. An approximate equivalent compass direction is also listed. Some events are so faint or subtle that a PA could not be measured.

^dElongation (angular distance) from Sun; first observed to last observed.

(9) Morphological type, (10) Angular speed of CME (degrees/hour), (11) Point-P speed (km/sec), and (12) Elongation range of CME (degrees).

[26] As discussed above, the dates, times and locations of each CME refer to the position of its center when first detected. This central axis is listed in column 6 in both degrees (measured counterclockwise from ecliptic north) and as a compass direction. Angular span is the difference in PA between the sides of the CME structure. This is often a lower limit because of interference by particles, auroral light, and saturated or shutter-closed frames.

[27] Two speeds are listed for each CME: an angular speed based on the sequentially increasing value of ε (column 10) and a speed based on the point-P approximation (column 11). Both use the ε versus time data of the CME central axis as measured on consecutive NRTD maps. (The approximate average PA of this axis is given in column 6.) The angular speed is derived from a radial, linear fit to ε versus time for a given CME; the range of ε over which the CME is tracked is given in column 12. (Some examples of ε -time plots and linear fits are shown in Figures 6b, 7d, and 8b). Speeds based on the point-P approximation [e.g., Howard *et al.*, 2006] depend on the assumption that the CME front can be approximated as a Sun-centered circular arc and that the maximum density along the line of sight occurs at the closest approach point

of that line of sight to the Sun, i.e., at the tangent point, P, of the arc. The distance from the Sun to P then is equal to the sine of the observed ε , since SMEI is at 1 AU from the Sun, and the speed is the change of this distance with time, converted to appropriate units, here km/sec. Although we have determined a point-P “speed” for all SMEI CMES, this approximation is strictly valid only for CMES whose trajectory is directed toward the Earthward hemisphere of the sky. However, various considerations argue that SMEI is most sensitive to light from CMES in the Earthward hemisphere and, possibly, in its vicinity. Thus the point-P approximation provides a reasonable first-order approximation to the true speeds of CMES viewed by SMEI. This approximation, however, will usually provide only lower limits to the true distances and speeds.

[28] Table 2 summarizes a statistical analysis of the CMES from Table 1 together with equivalent values from the SOHO LASCO coronagraphs obtained over the same time period (S. Yashiro, private communication, 2005). During the 1.5 years of SMEI observations considered in this paper, the observed CME occurrence rate was 0.254 CMES/day (139 CMES/547.5 days). Since early in the mission, SMEI has maintained a “duty cycle” for nominal operations of $\sim 85\%$. Correcting for this duty cycle yields a corrected CME occurrence rate of 0.30 CMES/day. However, unlike typical coronagraphs, this SMEI rate

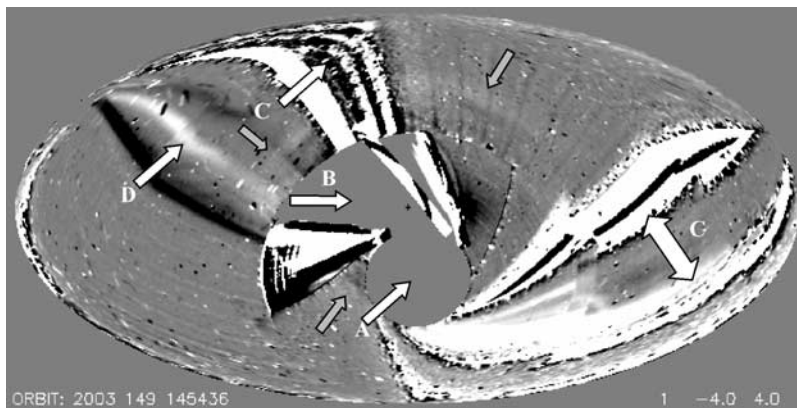


Figure 4. A single-orbit difference image showing both a CME (shaded arrows) and the main obscuration effects viewed by SMEI (open arrows). Lettered arrows point to the following: missing data resulting from zone of exclusion near Sun (A), camera 3 frames that are shuttered because of bright sunlight (adjacent white/black areas have sunlight-saturated CCD pixels that are not bright enough to close the shutter) (B), particle enhancements from both the polar zones and SAA (C), and auroral light (D). The CME appear as arcs seen in three unobscured areas of the inner heliosphere. This was the first Earthward-directed halo CME observed by SMEI, on 29 May 2003 (see Figure 8). Brightness range of the image is from -4 to $+4$ ADUs.

Table 2. Summary of Statistical Results of SMEI CMES

Parameter	Instrument	Observed Mean	Corrected Mean	Range	Notes
Occurrence rate	SMEI	0.25	(>)0.30 CMES/day		
	LASCO	3.06	3.38		
	Helios 2	0.03	[0.27]		(Sunspot min.; 1976)
	Helios 1	0.31	[2.48]		(Sunspot max.; 1981)
	Cambridge IPS	0.29	[0.44]		
Duration	SMEI	16.3 hours		3.5–~70 hours	
	Helios 2	37			(1976–1979)
Span	SMEI	(>)40°		3°–113°	
	LASCO	60			(median = 42)
	Helios 2	53			(1976–1979)
Brightness	SMEI	1.7 S10		0.4–10 S10	
	Helios 2	2.3 S10		1.5–3.0 S10	(1976–1979)
Angular speed	SMEI	1.065°/hour		0.3–4.9°/hour	
Point-P speed	SMEI	473 km/sec		51–1611 km/sec	
		~500		(1976–1979)	
Plane-of-sky speed	LASCO	507			(median = 442)
Elongation Range	SMEI; first observed			17°–110°	
	SMEI; last observed			23°–142°	

should also be corrected for the varying areal coverage, which can be different for each of the three cameras. For example, while a given camera is being calibrated, data cannot be obtained from the other cameras. The importance of making some correction for areal coverage is illustrated by Figure 4, which shows that significant areas of the sky can be obscured (by particle hits and saturated or shuttered frames) on any given orbit and that these areas differ from orbit to orbit. Furthermore, the sunlight-obscured area affects only the sunward camera and moves with the seasons. The SMEI duty cycle estimate also must include data loss from lunar light contamination and auroral light [Mizuno *et al.*, 2005]. We are in the process of determining the SMEI duty cycle, including areal obscuration effects. Thus the CME occurrence rate in this paper is preliminary and an underestimate of the true SMEI rate. In addition, we expect that fainter CMES will be detected in future, fully calibrated SMEI sky maps.

[29] The LASCO CME occurrence rate is about an order of magnitude higher than this preliminary SMEI rate. (LASCO rates for the current cycle are also about a factor of 2 higher than those of previous coronagraphs, suggesting that LASCO is a more sensitive coronagraph than previously flown.) Thus SMEI sees only a fraction of the CMES identified in the LASCO data. We discuss next some possible reasons for this difference from a comparative study of the CMES seen in both instruments.

[30] Table 2 also includes CME rates in the inner heliosphere observed by the Helios 1 and 2 photometers from solar minimum in 1976 to maximum in 1981. Two rates for each period are listed, one the observed rate and the other a rate adjusted for possible missed events. As Webb and Howard [1994] showed, the CME rate tends to track the sunspot number in phase and varies by about a factor of ten over a cycle. The preliminary SMEI rate agrees with the Helios adjusted rate at minimum and the observed rate at maximum, although Webb and Howard argued that only the adjusted Helios rates agreed well with those of the Solwind and SMM coronagraphs during that period. Table 2 also includes the rate of transients observed by the Cambridge IPS array at Lord’s Bridge, England, from February 1980 to March 1981, adjusted for “visibility” [Tappin, 1984]. Interestingly, this rate is comparable to the SMEI CME rate and to Helios at maximum, also in 1981.

[31] Finally, Table 2 also shows the mean values and ranges of SMEI CME durations, angular spans, brightnesses and speeds and their comparison with equivalent LASCO and Helios 2 results [Webb and Jackson, 1990]. Durations are the time differences between the first and last measurements made over the ε ranges in column 12, Table 1. The average duration of a SMEI CME was ~16 hours but some were observed for as long as three days. These durations tend to be lower limits as the CME might have been visible on the orbit before or after but no measurement could be made. The Helios CMES averaged 1.5 days in duration and ranged over 4 days, but these are biased because the CME was required to be detected in the north ecliptic pole photometer, implying that it had to encounter or pass north of the spacecraft. The SMEI CME angular spans or widths averaged 42° and ranged up to 107°. The mean span is shown as a lower limit because in many cases one or both “sides” of the CME was obscured.

[32] The mean CME brightness was 1.25 ADU with a range of 0.2–6.0 ADU. Using the Buffington *et al.* [2004] conversion factor yields a mean brightness of 2.3 S10 with a range of ~0.4–10 S10. The mean SMEI CME brightness is the same as that measured for Helios 2 CMES from 1976–1979 which, however, varied over the cycle. The mean point-P speed can be approximately compared with the mean and median values for LASCO CMES over the same period and with Helios 2 speeds from 1976–1979. The three mean CME speeds are very similar. This is surprising because SMEI sampled only a fraction of the LASCO CMES, but at distances considerably farther from the Sun. Helios and SMEI CME speeds were determined over similar distance ranges. Helios also used an approximation similar to point-P, however, the speeds could only be estimated from the peak passage times of the material between pairs of photometers.

[33] Figure 5 shows histograms of the observed elongations of the SMEI CMES: (1) when the CME is first observed by SMEI with an ε range from 17 to 110° (Figure 5a) and (2) when the CME is last observed by SMEI with a range from 23 to 142° (Figure 5b). Because of the 20° zone of exclusion around the Sun, SMEI cannot detect CMES with smaller ε . About 1/3 of all CMES observed by SMEI could be tracked far from Sun to $\varepsilon \geq 70^\circ$.

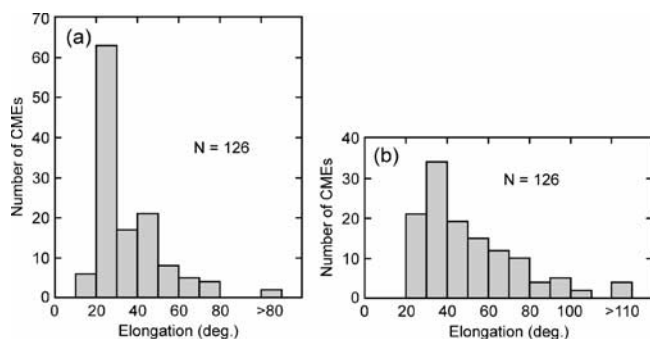


Figure 5. Histograms of the observed elongations of SMEI CMEs: (a) when the CME is first observed by SMEI with a range from 17° to 110° and (b) when the CME is last observed by SMEI with a range from 23° to 142° . About 1/3 of these CMEs can be tracked far from Sun (i.e., beyond $\sim 70^\circ$).

2.3. Illustrative Examples

[34] “Type” (column 9 of Table 1) refers to several morphologies for the SMEI CMEs: arc, loop, blob, V arc or halo. SMEI observed only four “V arc” events, which appeared as bent, V shaped or concave outward structures. The single “halo” event is the 28–29 May 2003 CME in which bright arcs appeared at similar elongations in all unobscured regions, implying the existence of a full halo CME [Tappin *et al.*, 2004]. A more interpretative scheme reveals seven classes: Limb CMEs, Erupting Prominences with CMEs, Earthward (halo) CMEs, Concave-outward

V-shaped CMEs, Multiple CMEs, Distant wide arcs and Miscellaneous. Examples of each of these are shown in Figures 6–10 and discussed next.

[35] Figure 6a is an example of a limb CME, one of two nearly identical, fast, loop events that likely were associated with active region NOAA no. 0365. (This active region had earlier been associated with the 28–29 May 2003 halo CME shown in Figures 4 and 8 when the active region was near Sun center.) This eruption led to a circular loop CME seen in one LASCO C2 and two C3 images (inset Figure 6a). The loop’s location and width ($\sim 60^\circ$) are similar in both the LASCO and SMEI views. Figure 6b is the elongation versus time plot of the CME front. Assuming projection in the skyplane, the speeds of the front calculated from the LASCO (~ 1700 km/sec; G. Lawrence, private communication, 2003) and SMEI (~ 1450 km/sec) data agree reasonably well. Such bright, relatively fast CMEs occurring near the solar limb are fairly easy to detect in SMEI’s sunward camera and to correlate with solar surface events and LASCO CMEs since Thomson scattering is maximized for plasma orthogonal to the line of sight. However, we note that in SMEI images such limb CMEs fade rapidly and disappear as they move outward. Perhaps as many as half of the SMEI CMEs may be in this category, but a more precise accounting will depend on identifying the near-surface activity associated with each event.

[36] Figures 7a–7c shows a large erupting prominence-associated CME. In the SMEI difference images (Figure 7c), a faint band is followed by a series of brighter bands that may be the denser material associated with the prominence.

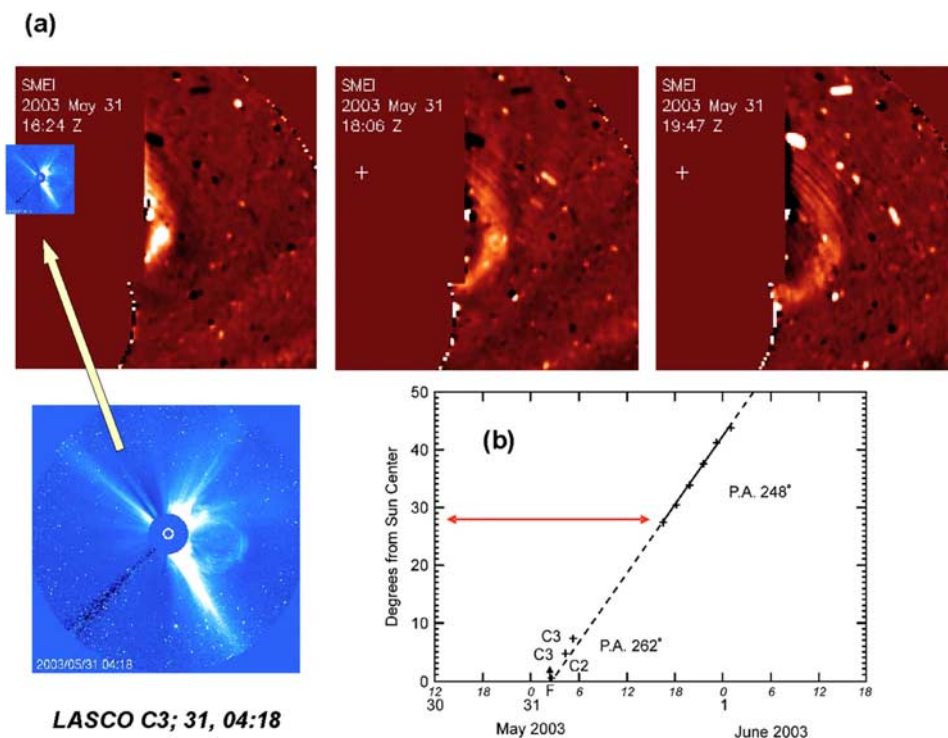


Figure 6. (a) Example of a limb CME on 31 May 2003 as viewed by SMEI. Event was associated with a 2B, M9.3 flare with onset at 02:15 and disk location $S07^\circ W65^\circ$. This led to a circular loop CME seen in LASCO (C3 image in inset). (b) Elongation versus time plot of the CME front seen in SMEI with $27^\circ < \epsilon < 44^\circ$. Linear fit extrapolation earlier in time matches well with the flare (F) onset and C2, C3 height times.

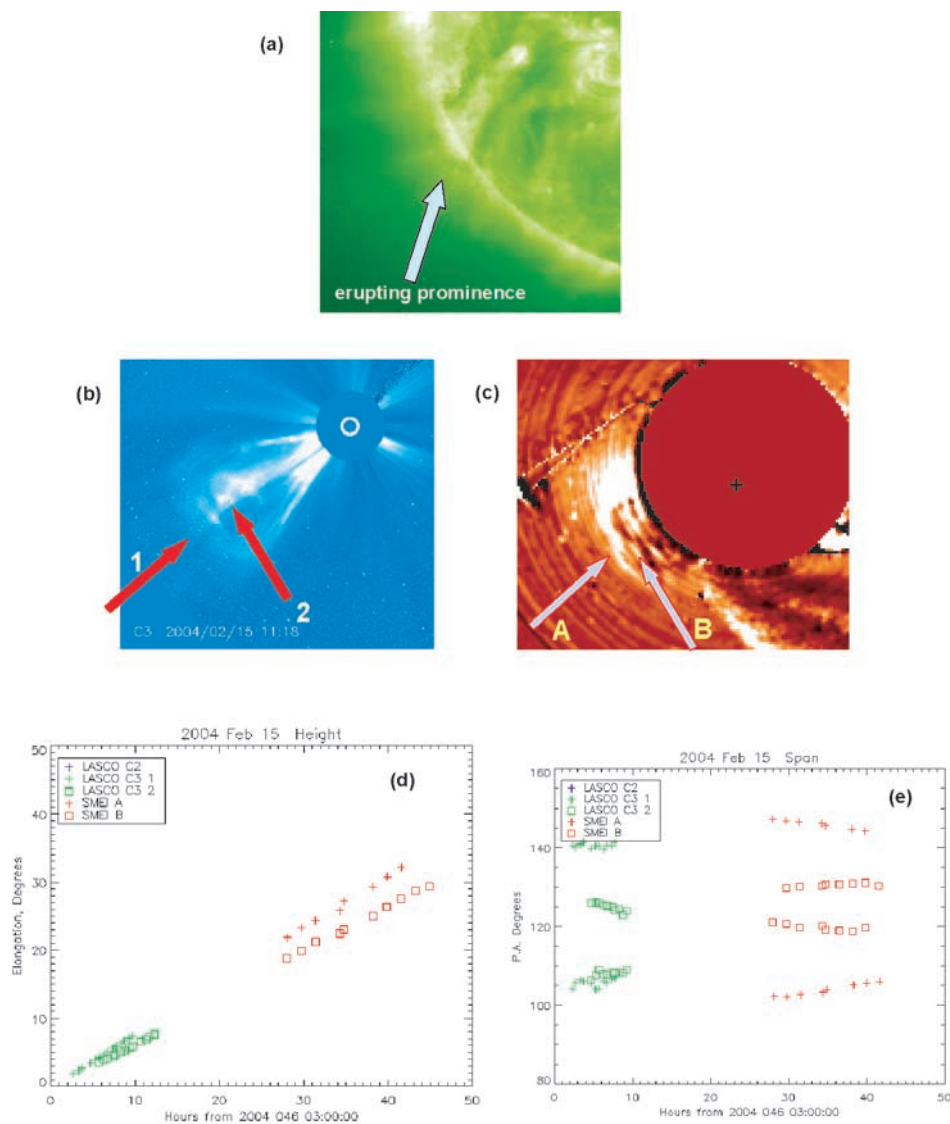


Figure 7. A large erupting prominence-associated CME on 15–16 February 2004. Shown are three views at progressively later times, in (a) EIT 195A on 15 February 02:00, (b) LASCO C3 on 15 February, 11:18, and (c) SMEI on 16 February, 15:29. The EIT image shows the rising prominence that becomes the core of the LASCO “three-part” CME. (d) Elongation versus time plot of the CME leading arcs in SMEI (A and B, red) between 22° and 33° and the leading loop, 1, and core, 2, in LASCO C3 (green). (e) The angular spans of these parts of the CME in the LASCO (green) and SMEI (red) FOV.

Preliminary studies of this CME and another on 19 February 2003 show that the angular spans of the CMES, including the inner portions, are comparable in the LASCO and SMEI fields of view [Figure 7e; Johnston *et al.*, 2005]. At least six of the 139 SMEI CMES appear to be of this class.

[37] Earthward directed CMES are associated with surface activity near the center of the Sun and normally appear in LASCO as circular halos completely surrounding the occulting disk. However, with SMEI we have observed only one probable complete halo CME: the 28–29 May 2003 event shown in Figures 4 and 8 and studied by Tappin *et al.* [2004]. We suspect that SMEI may typically detect only one or more arcs of CMES that begin as frontside halo CMES in LASCO. In a separate study summarized in section 2e, SMEI detected CMES prior to >80% of the moderate to

major geomagnetic storms during the 1.5 year period. There were 10 geoeffective SMEI CMES associated with the most intense ($Dst < -100$ nT) storms. The event in May 2003, the largest storm during the first half of the year, apparently involved two X-class solar flares and LASCO halo CMES, and the elongation versus time plot in Figure 8 shows that the two SMEI components had different trajectories. In terms of their relationships to 1 AU shocks and storms, perhaps as many as 40, or 30% of all the SMEI CMES may be Earthward-directed.

[38] Figure 9 shows four concave-outward, V-shaped CMES. Trailing concave-outward CME structures have previously been linked to the disconnection/reconnection of magnetic fields within or surrounding CMES and with magnetic flux ropes and prominence eruptions [e.g., Illing and Hundhausen, 1983; Webb and Cliver, 1995; Chen *et al.*,

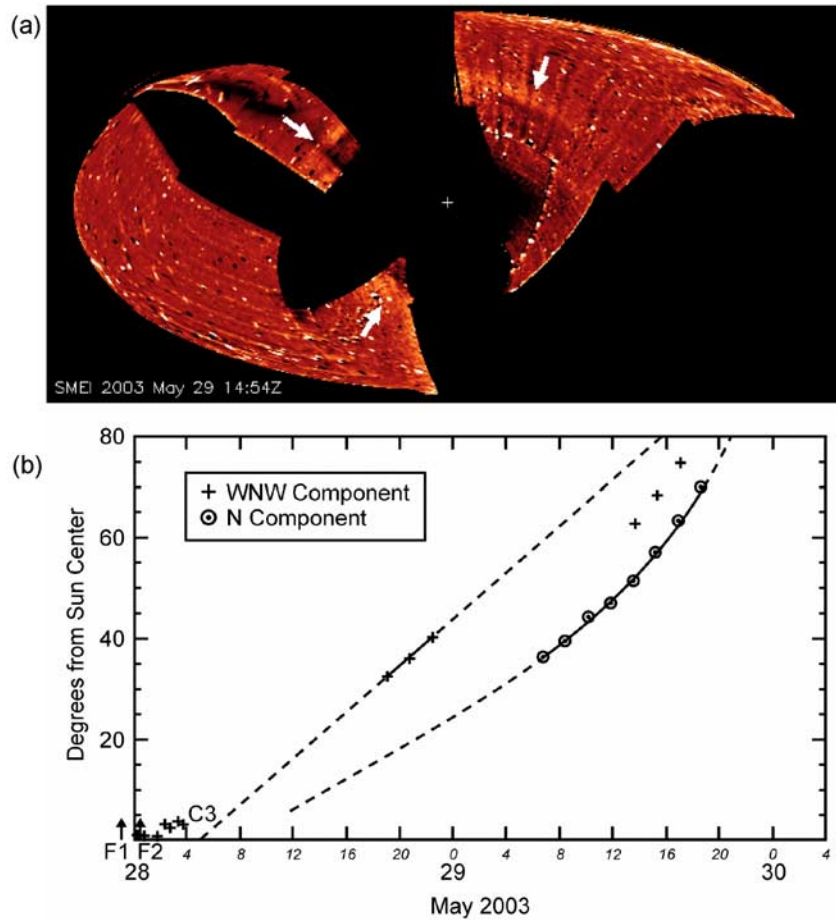


Figure 8. (a) The first and best example of Earthward-directed halo CMEs detected by SMEI. LASCO observed two nearly simultaneous halo CMEs associated with two flares: F1, an X1.3 on 27 May at 23:07 UT and F2, an X3.6 on 28 May at 00:27 UT. The later SMEI transient appeared as three contiguous arcs together covering over 150° of sky (arrows). (b) Elongation versus time plot showing that the SMEI components had different trajectories.

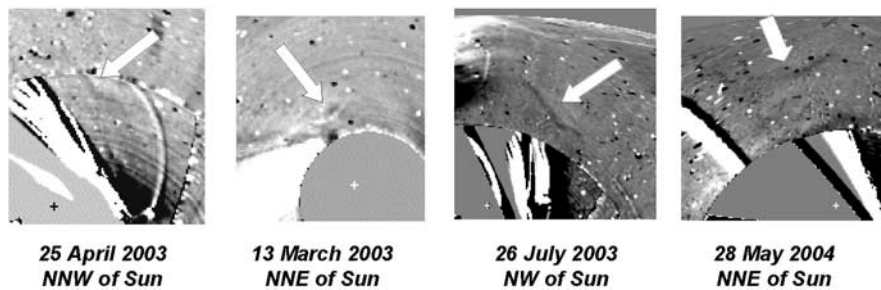


Figure 9. Orbital difference images of the four CMEs that SMEI detected as bent or shallow U or V-shaped, concave-outward structures which are unlike any others seen in the SMEI observations. All had moderate brightnesses and speeds and were seen over a wide elongation range from 17–72°. Three of the four events appear to have had associated LASCO CMEs with trailing concave-outward morphology but were otherwise not unusual. Two of these events, 25 April 2003 and 28 May 2004, were associated with frontside arcade formation and prominence eruptions. The Sun is located at the ‘+’ signs and the exclusion zone circle is 20° in radius.

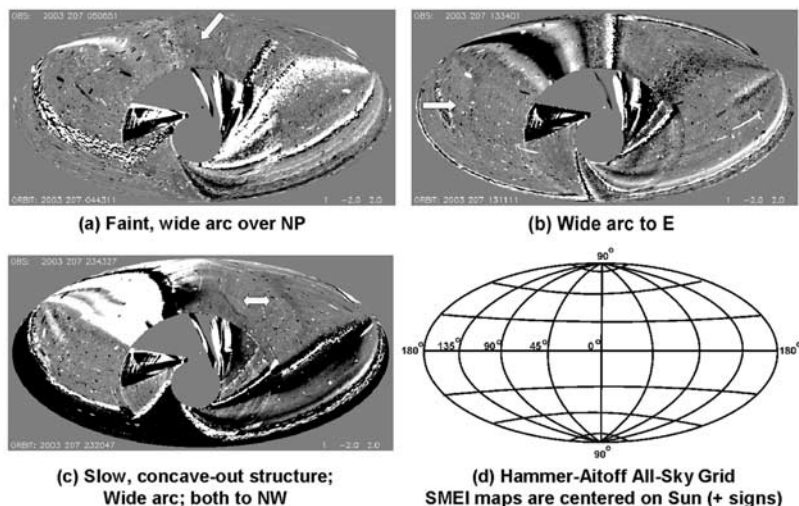


Figure 10. Examples of multiple CMEs and distant wide arcs. Several very wide moving arcs were observed to large elongations on 26 July 2003: (a) arc to the north northeast at 05:05, (b) wide arc to the east at 13:34, and (c) wide arc to the northwest at 23:43. Left arrowhead points to the concave-outward structure highlighted in Figure 9 on this day. (d) Sample Hammer-Aitoff all-sky grid.

1997; *Simnett et al.*, 1997; *Webb et al.*, 2003]. It is possible that SMEI observes these particular CME segments because they are denser than normal and/or are directed toward Earth.

[39] Figure 10 shows examples of the last two classes of CMEs from a very active period during 23–27 July 2003 when seven separate transients were detected in the NRTD movies. Several of these were very wide, moving arcs seen to large distances. Arrows point to three such arcs on 26 July. On this day there were four separate transients visible, the three arcs plus the concave-outward structure. Although faint and subtle in individual frames, these wide arcs are clearly evident in movies. Because of the Thomson-scattering geometry, these distant arcs could either be directed toward the Earthward hemisphere of the sky or in some cases could be near Earth. For example, the eastern arc in Figure 10b swept beyond 90° elongation through Camera 2 into Camera 1 at about the time a moderate geomagnetic storm began (peak on 27 July at 08:00). Indeed, Figure 10c shows large white and black areas that are the brightening auroral light caused by that storm. The northern (Figure 10a) and eastern (Figure 10b) arcs may be two parts of one CME structure, separated by a band of particle obscuration that would then extend more than 100° . We could find no obviously associated LASCO CMEs, particularly halos, during this period, although there were bright, but narrower events to the northeast on 25–26 July.

[40] The distant arc events are fairly common, comprising about 30% of all the SMEI events. Multiple events also occurred within a relatively short time during 1–4 March 2003, 28 May to 2 June 2003, 23–24 October and 27 October to 3 November 2003, 21–25 January 2004, and 29 March to 4 April 2004. A total of 36, or a quarter of all the SMEI events, occurred during these periods. Finally, as with CMEs observed by coronagraphs, there were many SMEI CMEs that do not fit easily into any of these categories. We note that these interpretations are based solely on the NRTD images; more events may be identified and different

interpretations of the currently identified events may be necessary when the fully calibrated data become available.

2.4. Comparisons With Solar Activity and LASCO CMEs

[41] Studies comparing SMEI CMEs with solar activity in general and with LASCO CMEs in particular are in a preliminary stage. Some of the authors have previously studied the associations between CMEs observed by various coronagraphs and surface or near-surface solar activity [*Webb and Hundhausen*, 1987; *Webb and Jackson*, 1990; *Webb and Howard*, 1994]. These studies must deal with the gap in time and distance between solar surface and low coronal (50,000–100,000 km) activity, and the appearance of the CME in the coronagraph FOV (nominally $>400,000$ km). Height time plots are generally used to extrapolate backward from the leading edge of the CME and forward from the solar activity to arrive at an “association”. Determining objective criteria for such associations can be challenging. Although this process can be straightforward for bright, fast events, this may be difficult or even impractical for fainter and/or slower CMEs.

[42] During the SMEI mission we have been fortunate to have SOHO, especially the LASCO and EIT instruments, and the Transition Region and Coronal Explorer (TRACE) spaceborne imaging observations of the solar surface and lower atmosphere. However, the SMEI near-Sun exclusion zone (approximately $\geq 20^\circ$, see sections 1b and Figures 4 and 5a above) requires extrapolation over an even larger time-distance gap than that between the Sun and LASCO for associations. The outer LASCO coronagraph, C3, views out to only 7.5° ($30 R_s$), leaving a gap of $\geq 12^\circ$ between this and the SMEI observation of a given CME.

[43] *Simnett* [2005] and *Simnett and Kahler* [2005] examined the LASCO data for periods corresponding to likely onset times of the SMEI CMEs at the Sun for all the SMEI events observed in 2003. Two criteria were used to establish an association: (1) The PA of the LASCO event

should be within 20° of the SMEI PA (we also noted events which lay 40° outside this range); and (2) the distance-time profile for the SMEI event should match the onset of the candidate LASCO event to within ± 6 hours. For the majority of the associations both criteria were easily met. Of the 88 SMEI events identified on the NRTD maps during 2003 (Table 1), the distance-time profiles were difficult to establish for two, and two others were probably continuations of earlier events when SMEI orbital data were missing. Another four events occurred when LASCO was not observing. Of the remaining 80 events, 11 had no detectable coronal transient in LASCO imagery and one event, seen by SMEI on 21 November and associated with a LASCO CME on 20 November, did not have a credible speed even though it satisfied the selection criteria defined above, thus making this association unlikely. Another 10 had extremely faint associated coronal transients that could only be seen in running difference images.

[44] Of the 69 events having an association, 57 were matched in position angle to within 10° , which is in good agreement since the typical width of a SMEI event is $>10^\circ$. For 11 events the LASCO position angle was between 11° and 20° of the center of the SMEI event. Only the 10 July 2003 event lay outside this range, with a position angle difference of 28° between LASCO and SMEI. For the faint or nonexistent LASCO events, no candidate event was within 60° of the SMEI transient.

[45] Summarizing, 71% (57 of 80) of SMEI CMES observed in 2003 were associated with obvious LASCO CMES, another 14% (11 of 80) were associated with very faint LASCO CMES, and the remaining 15% (12 of 80) had no visible associated LASCO event. This raises the question of how CMES become visible as they propagate through the interplanetary medium. One possibility is that an erupting magnetic structure which initially contains very little excess mass picks up mass by the so-called “snowplow effect” while traveling through the inner heliosphere [Howard and Tappin, 2005]. It is also known that many LASCO CMES apparently fade out and disappear below about $10 R_s$ [Gopalswamy, 2004]. Other possibilities are that SMEI is detecting the formation of corotating interaction regions, and/or dense regions associated with the interplanetary shock or its sheath that lies ahead of the CME itself.

[46] We have begun a more detailed comparison between LASCO and SMEI that entails the more difficult forward extrapolation from LASCO CMES to SMEI CMES. We know statistically that SMEI observed fewer CMES than LASCO over the same time period (see Table 2). On the other hand, while many bright and even fast CMES in the LASCO FOV are without SMEI counterparts, some SMEI transients are very faint or not visible at all near the Sun. We expect future studies will lead to a better understanding of the evolution of CMES and their propagation through the inner heliosphere.

2.5. Earthward Directed CMES and the Implications of SMEI Observations for Space Weather

[47] CMES are a primary cause of severe space weather at Earth since they trigger geomagnetic storms that damage space and ground-based assets. Such storms initiate a plethora of adverse effects, including increases in trapped

magnetospheric particles, degraded satellite communication, navigation, and surveillance systems, increased drag and deterioration of satellite altitude control, and destructive surges in ground power grids. For example, the “Halloween” 2003 storms caused a wide variety of anomalies [see Webb and Allen, 2004], including loss of a Japanese satellite, a first ever FAA high-radiation dosage alert for high-altitude aircraft, and a power system failure in Sweden. Astronauts in the International Space Station were forced to seek shelter. These hazardous storms are difficult to forecast and false alarms are frequent [Josefyn, 1995]. Early detection of potentially damaging Earth-directed CMES is needed to protect space assets and maintain stable communications.

[48] SMEI’s primary purpose as a U. S. Air Force experiment is to demonstrate the ability to track CMES from near the Sun to Earth, thus providing a new capability for forecasting storms. SMEI has accomplished this initial objective by detecting a number of geoeffective CMES at elongations of 20° – 30° , equivalent to $\sim 1/3$ of the distance from the Sun to Earth. Depending on the speed of the CME front, these distances correspond to advance warning times of 10 hours to 2 days. Because of a data latency time of 12–24 hours during most of its mission, SMEI has not yet been used to make real-time forecasts. However, these results do provide proof-of-principle that SMEI could detect even fast Earthward moving CMES at least one day before their arrival and, therefore that an operational version could provide significant early warnings of storms. Such heliospheric imaging observations, including IPS data [Manoharan 2006], can provide added value for space weather forecasting when assimilated into physics-based heliospheric models, such as the operational HAFv.2 model [Fry et al., 2003; Dryer et al., 2004; McKenna-Lawlor et al., 2006].

[49] Tappin et al. [2004] described the first Earth-directed CME detected and analyzed in the SMEI data that occurred in late May 2003 (Figures 4 and 8). This fast transient appeared in the NRTD images at $\sim 30^\circ$ elongation and ~ 15 hours before it passed over the Earth on 29–30 May causing a major geomagnetic storm. During late October and early November 2003, an unusual series of major solar events produced high levels of energetic particles in geospace and led to large geomagnetic storms on 28–30 October [e.g., Murtagh et al., 2004; Webb and Allen, 2004; Dryer et al., 2004]. Jackson et al. [2006] described the SMEI observations and 3D reconstructions of the 28 October CME. Figure 11 shows Sun-centered, ecliptic “fisheye” sky maps derived from the edited time series and 3D reconstructions of the SMEI data for this event. Although LASCO observed this as a complete halo with a bright prominence eruption to the south, the CME viewed by SMEI showed two fast, dense portions of the ejecta near Earth.

[50] We have performed two independent studies of SMEI’s capability to detect and track CMES that subsequently caused major storms at Earth. First, we examined the sources of the most intense (peak $Dst < -100$ nT) geomagnetic storms during a 2-year interval. There were 14 such storms and SMEI had suitable data during 12 of them. For 10 of those 12 storms (83%), SMEI observed associated Earthward-directed CMES. During all 12 storms SMEI also observed the bright auroral light associated with the storm

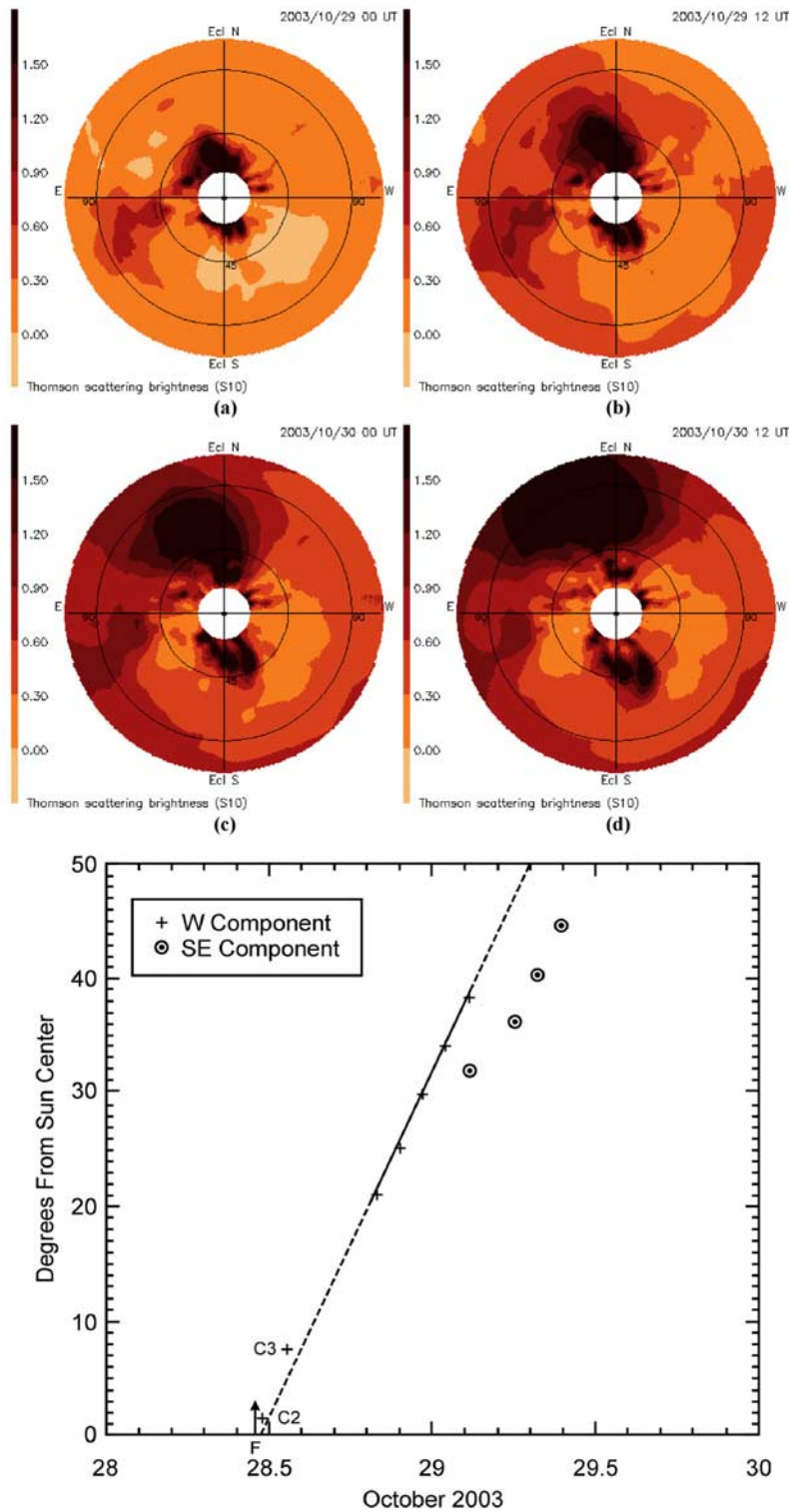


Figure 11. (top) Sun-centered ecliptic fish-eye sky maps derived from the edited time series and 3D reconstructions [Jackson *et al.*, 2006] shown out to 110° elongation as viewed from SMEI for the 28 October 2003 CME. (a–d) The faster portion of the CME directed toward Earth is to the solar northeast and begins to engulf Earth (reach 90°) about midday on 29 October. Simultaneously, the large prominence-associated ejecta to the south reached just beyond 45° elongation. Different parts of the CME can be observed moving outward over the next two sky maps. (bottom) Elongation time plot that shows at least two trajectories of this material in the NRTD maps. Linear fit extrapolation of the western component matches well with the flare (F) onset and C2, C3 height times.

(e.g., Figure 4). The mean time difference between the first SMEI observation of the CME and the arrival of the associated shock at Earth was 18.6 hours, and 29.25 hours until the storm onset. The second study included all moderate or greater storms (peak $Dst < -60$ nT) over a similar 2-year time period. For 85% (39 of 46) of these storms, SMEI detected a CME within 2 days prior to the storm onset. The main conclusion from these studies is that SMEI can detect the CMEs causing most major geomagnetic storms, from 3/4 of a day to 2 days before storm onset, and thus provide early warning of their arrival.

3. Discussion

3.1. Summary of CME Results

[51] The main statistical results of the analysis of the 139 CMEs observed over the first 1.5 years of the SMEI mission are summarized in Table 2. The SMEI CME occurrence rate, corrected for duty cycle, is about 1/3 CMEs/day. (Note that this rate is based only on the NRTD observations and the temporal duty cycle and is therefore preliminary.) The LASCO rate for the same time period is about an order of magnitude higher. The rates of CMEs in the inner heliosphere can be more appropriately compared with those observed by the Helios 1 and 2 photometers from solar minimum in 1976 to maximum in 1981. The preliminary SMEI CME rate agrees with the Helios adjusted rate at minimum and the observed rate at maximum. Clearly, SMEI sees only a fraction of all eruptions identified as CMEs in the LASCO data, and we are currently comparing CMEs observed with both instruments to characterize the differences.

[52] We examined the appropriate LASCO data for evidence of CMEs corresponding to the SMEI events observed in 2003. We found that 71% of the SMEI CMEs were associated with obvious LASCO CMEs, 14% with very faint LASCO CMEs, and the remaining 15% with no associated LASCO event. That SMEI observes CME material in the inner heliosphere that is not visible near the Sun is an important finding that merits further study. Conversely, SMEI observed fewer CMEs than LASCO over the same time period.

[53] The morphological types we assigned to the SMEI CMEs were arc, loop, blob, V arc or halo. A more interpretative classification expands these into seven categories: Limb CMEs, Erupting Prominences with CMEs, Earthward (halo) CMEs, Concave-outward V-shaped CMEs, Multiple CMEs, Distant wide arcs and Miscellaneous. The most common classes were limb CMEs, distant wide arcs and Earthward-directed CMEs. The Earthward events are of the most interest for detecting and tracking geoeffective interplanetary disturbances (see section 3.3).

[54] The average duration of the CMEs observed by SMEI was ~ 16 hours with a maximum of about three days. The Helios CMEs averaged 1.5 days in duration and ranged over four days, but were biased toward longer durations. The SMEI CME angular spans or widths averaged 42° , ranging up to 107° . However, the mean span is likely a lower limit because of obscuration of the sides of many CMEs. This could explain why the mean SMEI CME angular spans were less than those measured by LASCO and Helios 2. The mean brightness of a SMEI CME was

2.3 S10 units, the same as that measured for Helios 2 CMEs from 1976–1979. The mean angular speed of SMEI CMEs was $1.1^\circ/\text{hour}$. A “point-P” approximation method yielded a mean CME speed of ~ 500 km/sec., comparable to the mean and median values for LASCO CMEs over the same period and to Helios 2 CME speeds. The observed elongations of the first SMEI CME observation ranged from 17° to 110° , and the maximum to which SMEI could track CMEs was 142° .

[55] Finally, SMEI accomplished its primary objective of demonstrating the feasibility of improving forecasts of geomagnetic storms by detecting dozens of geoeffective CMEs at distances equivalent to $\sim 1/3$ of the distance from the Sun to Earth, allowing scientists to track them on distance-time plots and to estimate arrival times at Earth. SMEI observed more than 80% of the Earthward-directed CMEs that were associated with large storms over a 2-year period proving that, given adequate data latency, a SMEI-type instrument can detect even fast Earthward CMEs from ~ 10 hours to ~ 2 days before their Earth arrival. Detecting and tracking CMEs in this distance range is a new capability that, when combined with other space environment sensors and physics-based heliospheric models, promises to greatly enhance our ability to forecast and study space weather.

3.2. CMEs in the Heliosphere

[56] Before SMEI there were few observations capable of helping us understand the development and propagation of transient disturbances through the inner heliosphere. The SMEI near-real-time images show that CMEs appear more structured nearer the Sun, typically at ε of $20\text{--}30^\circ$, than farther away. Many initially bright CMEs fade and even disappear completely before exiting the sunward Camera 3 FOV. Similarly, LASCO has observed that CMEs are often brighter and more structured nearer the Sun in C2 than when viewed farther out and later in C3. Even so, the morphology of some highly structured CMEs in LASCO can be traced into the SMEI FOV despite the gap of some $70 R_s$ between the instruments (see Figure 7).

[57] As noted above many of the SMEI CMEs appear as broad arcs far from the Sun, usually in Camera 2 or 1. It is not clear why CMEs are more structured nearer the Sun and arc-like farther away, but viewing geometry and Thomson-scattering effects undoubtedly play roles. Additionally, an expanding CME may sweep up ambient mass, the so-called snowplow effect, while traversing the inner heliosphere. Another possibility is that SMEI is more sensitive to the enhanced density in the compressed and turbulent “sheath” region that is sandwiched between a transient interplanetary shock and the leading edge of the CME which trails it.

[58] Observational and theoretical work [e.g., *Smith and Dryer, 1990*] suggest that the deceleration of ICMEs and their associated shocks is a function of their velocity with respect to the background solar wind speed; that is, the greater the relative speed difference, the larger is the deceleration. One approach to understanding the propagation of heliospheric transients and in particular the processes that either decelerate them or act to prevent the deceleration, is to connect SMEI observations of a CME near the Sun to observations at a distant spacecraft, in particular Ulysses. Some LASCO CMEs have been associated with events seen at Ulysses. However, because of the large distance between

the edge of the LASCO FOV at 30 Rs and Ulysses at several AU, and uncertainties in the actual longitude of the CMES, these identifications are often ambiguous. Recently, however, *Tappin* [2005] studied a SMEI CME on 7 April 2003 (day 097 in Table 1) that was first seen in LASCO on 5 April and tracked by SMEI out to Ulysses. With these measurements, *Tappin* [2005] was able to calculate the deceleration of the transient and compare it with various models of the deceleration process. It was found that both a simple snowplow model and an aerodynamic drag model predict a more rapid deceleration than is observed, and therefore some driving force is needed over an extended distance to account for the motion derived for this transient.

[59] Thus the SMEI observations are useful both for studying the propagation and evolution of heliospheric structures as they interact with each other and with the ambient solar wind, and for forecasting the arrival of these structures at Earth. However, interpreting these data is complicated because they are a line-of-sight integration of an a priori unknown 3D distribution of outward moving material in the solar wind at an uncertain location relative to the Sun and Earth. One way to resolve the ambiguity is to assume that structures are located in the plane of the sky, which provides useful information about, e.g., corotating structures. However, when a transient structure such as a CME is observed across a large range of solar elongations, the 2D plane-of-the-sky assumption breaks down because the structure occupies an expanding, 3D volume of space with significant extensions along a given line of sight at all times.

[60] The UCSD group has developed a technique to reconstruct 3D solar wind structure from remote sensing data at a single location by exploiting kinematic outward motion to yield the missing distance information. The 3D results can be viewed from any direction, and the heliospheric structure locations measured in heliographic coordinates and solar distance as a function of time. This technique has been used successfully to analyze CMES using IPS data, and Helios and now SMEI Thomson-scattering observations. SMEI 3D reconstructions have been made of the 28–29 May 2003 and 28–29 October 2003 CMES [*Jackson et al.*, 2006]. Although LASCO observed the 28 October event as a complete halo with a bright prominence eruption to the south, the heliospheric manifestation as viewed by SMEI revealed two fast, dense portions of the ejecta as it neared Earth. One part was the prominence passing to the south of Earth, and the other part was to the northeast and engulfed Earth by midday on 29 October. We were able to track the event from its first measurement approximately 20° from the solar disk until it vanished from the SMEI FOV on the side of Earth opposite the Sun.

[61] Forbush decreases in neutron monitor counting rates are caused by enhanced magnetic fields in interplanetary shocks and solar ejecta that shield the Earth from galactic cosmic rays. The solar origins of those ejecta can be observed as CMES in coronagraphs, but their propagation through interplanetary space to Earth has not been previously observable. The SMEI experiment now allows searches for the white light signatures of interplanetary CMES (ICMES) responsible for Forbush decreases, including the ability to track their propagation through the inner

heliosphere out to distances beyond 1 AU and to distinguish those that hit Earth from those that do not. *Kahler and Simnett* [2005] selected all Forbush decreases of $\geq 2\%$ observed with the Oulu, Finland neutron monitor and found excellent associations with SMEI CMES. Furthermore, for each of the SMEI CMES they also found an associated LASCO CME.

[62] Since SMEI routinely views nearly the entire sky in broadband white light, it has detected some bright objects in the inner heliosphere that are also visible in Earth and space-based telescopes, such as bright comets and asteroids. In May 2004 SMEI observed spectacular tail disconnections of Comets Linear (C/2002 T7) and Neat (C/2001 Q4). Since SMEI was designed to be sensitive to the very low light levels from CMES, it can observe and track the very faint comet remnants over much longer temporal and spatial scales than are possible from the ground. *Kuchar et al.* [2004] found that a CME front was the probable cause of the Comet Neat tail disconnection on 5–6 May 2004, which began on 5 May when SMEI observed a broad and wide transient arc sweeping past the comet nucleus and tail (Table 1, DOY 125, 2004).

3.3. Concluding Remarks

[63] The final goal of the SMEI “pipeline” processing is to combine the individual SMEI image frames into a heliospheric sky map for every spacecraft orbit. These maps are generally displayed in Aitoff or fisheye projections with an angular resolution of 1° and the orbital time cadence of 102 min. The AFRL pipeline processing produces “quick look” heliospheric maps that demonstrate the feasibility of detecting and tracking solar mass ejections in near-real time. UCSD processes the data to produce sky maps that approach the full photometric and angular resolution design limits of SMEI. These maps will be considered fully calibrated and will facilitate the best quantitative analysis of the SMEI data. They will also be used to model heliospheric density structure using the 3D reconstruction techniques under development at UCSD.

[64] The UCSD scheme maintains the highest angular and photometric resolution of the SMEI data through the initial processing and formation of the all-sky maps [*Hick et al.*, 2005]. This permits removal of most of the high-energy particle hits, space debris, and hot or “flipping” pixels from the data. A lower-resolution sidereal sky map is then generated, from which bright stars, background stars, and the modeled zodiacal cloud are removed. The final maps can be output in any convenient sky coordinate system, such as the Sun-centered Aitoff or fisheye projections. Time series at selected sidereal locations are extracted and processed further to remove the bright aurora, variable stars and other unwanted signals. These time series of the heliospheric Thomson scattering brightness can then be used in the 3D tomographic reconstructions. Work is underway to streamline the processing scheme so that fully calibrated heliospheric maps can be made available in near-real time. The final goals of this effort are to automate the removal of bright aurora, variable stars and other unwanted signals, and produce 3D reconstructed maps.

[65] We briefly mention other studies involving SMEI data that are ongoing or planned for the near future.

[66] 1. During the next several years there will be a number of periods when the Ulysses spacecraft will be at favorable positions for joint LASCO-SMEI-Ulysses observations of ICMEs. Data taken during these periods will be examined to study the kinematics and propagation of interplanetary transients.

[67] 2. The low-frequency radio observations on Wind/WAVES provide important spectral and directional information related to the propagation of CMEs through interplanetary space. SMEI now allows the tracking of CMEs simultaneously in white light and radio from the corona to 1 AU [see *Reiner et al.*, 2005]. These techniques will also be applicable to CMEs observed by the twin STEREO SWAVES instruments to be launched in 2006.

[68] 3. The UCSD 3D reconstruction technique using SMEI data to provide estimates of interplanetary densities (section 3.2) can be improved by including IPS velocity data in the analysis. Jackson and colleagues are working with the STELab group to accomplish this and will continue to study coincident events during the STELab IPS observing season, typically from April through December of each year.

[69] 4. The Hakamada-Akasofu-Fry solar wind prediction model (HAFv2: *Hakamada and Akasofu* [1982], *Fry et al.* [2001]) is driven by solar observations and provides temporal profiles of solar wind parameters, IMF plots to ≥ 2 AU, and synthetic skymaps of polarization brightness for comparison with heliospheric imagers such as SMEI and STEREO. Solar source surface maps provide the inner boundary conditions for HAFv2 to characterize ambient solar wind conditions. *Fry et al.* [2003] determined that the largest source of error in predicted shock arrival time is the estimate of initial CME/shock speed at the Sun. SMEI observations of CME speeds are now used as input to the HAF model to evaluate possible improvements in forecast skill. HAFv2 may also be incorporated into the UCSD computer tomography technique [e.g., *Jackson et al.*, 2005] to improve HAFv2's ability to characterize the global heliosphere.

[70] When the SMEI data are fully calibrated, we should be able to measure other heliospheric structures including the compressed plasma associated with shock waves that are driven ahead of CMEs, steady state features that corotate with the Sun such as streamers and magnetic sector boundaries, the zodiacal light dust cloud and the Gegenschein. These heliospheric features, as well as CMEs and comets, were well observed by the Helios white light photometers and should also be easily observed by SMEI. As a byproduct of its main science goals, SMEI is providing a unique long-term database of discrete variable astronomical phenomena, including variable stars, extrasolar planet transits, novae and supernovae. Finally, SMEI is now imaging the heliospheric plasma in which other spacecraft are immersed, such as ACE, Wind and SOHO near Earth, deep space spacecraft such as Ulysses and, perhaps, in the future NASA's STEREO, Solar-B and SDO missions. Thus the SMEI observations can provide context not only for the in situ density observations, but also for other CME-associated plasma and magnetic field observations. If SMEI continues to operate successfully, the all-sky image and 3D reconstruction maps will be available during the STEREO mission providing important contextual information for

heliospheric CMEs and corotating structures observed by the SECCHI imaging instruments and measured by the in situ instruments on each spacecraft.

[71] **Acknowledgments.** SMEI is a collaborative project of the U.S. Air Force Research Laboratory, NASA, the University of California at San Diego, the University of Birmingham, U.K., Boston College, and Boston University. Financial support has been provided by the U.S. Air Force, the University of Birmingham, and NASA. Details about the SMEI instrument can be found at <http://www.vs.af.mil/factsheets/SMEI.swf>, and current and archival images and movies and presentations can be found at <http://smei.nso.edu/>. The work at UCSD was supported by AFRL contract FA8718-04-C-0050, NSF grant ATM-0331513, and NASA grant NAG5-134543. D.F.W., T.A.K., and D.R.M. were supported at Boston College by AFRL contracts AF19628-00-C-0073 and FA8718-04-C-0050. The work of S.J.T. was supported under contract F61775-02-WE043 to the University of Birmingham.

[72] Amitava Bhattacharjee thanks John Raymond and Murray Dryer for their assistance in evaluating this paper.

References

- Brueckner, G. E., et al. (1995), The large-angle spectroscopic coronagraph (LASCO), *Sol. Phys.*, *162*, 357.
- Buffington, A., B. V. Jackson, and P. P. Hick (2003), Calculations for, and laboratory measurements of a multistage labyrinthine baffle for SMEI, in *Innovative Telescopes and Instrumentation for Solar Astrophysics*, edited by S. Keil and S. Avakyan, *Proc. SPIE Int. Soc. Opt. Eng.*, *4853*, 490.
- Buffington, A., B. V. Jackson, and P. P. Hick (2004), Systematic error reduction and photometric calibration for the solar mass ejection imager, *Eos Trans. AGU*, *85*(47), Fall Meet. Suppl., Abstract SH11A-07.
- Buffington, A., B. V. Jackson, and P. P. Hick (2005), Space performance of the multistage labyrinthine SMEI baffle, in *Solar Physics and Space Weather Instrumentation*, *Proc. SPIE Int. Soc. Opt. Eng.*, *5901*, 590118, doi:10.1117/12615526.
- Buffington, A., D. L. Band, B. V. Jackson, P. P. Hick, and A. C. Smith (2006), A search for early optical emission at gamma-ray burst locations by the solar mass ejection imager (SMEI), *Astrophys. J.*, *637*, 880.
- Chen, J., et al. (1997), Evidence of an erupting magnetic flux rope: LASCO coronal mass ejection of 1997 April 13, *Astrophys. J.*, *490*, L191.
- Delaboudiniere, J.-P., et al. (1995), EIT: Extreme-ultraviolet imaging telescope for the SOHO mission, *Sol. Phys.*, *162*, 291.
- Dryer, M., Z. Smith, C. D. Fry, W. Sun, C. S. Deehr, and S.-I. Akasofu (2004), Real-time shock arrival predictions during the "Halloween 2003 Epoch", *Space Weather*, S09001, doi:10.1029/2004SW000087.
- Eyles, C. J., G. M. Simnett, M. P. Cooke, B. V. Jackson, A. Buffington, P. P. Hick, N. R. Waltham, J. M. King, P. A. Anderson, and P. E. Holladay (2003), The Solar Mass Ejection Imager (SMEI), *Sol. Phys.*, *217*, 319.
- Fry, C. D., W. Sun, C. S. Deehr, M. Dryer, Z. Smith, S.-I. Akasofu, M. Tokumaru, and M. Kojima (2001), Improvements to the HAF solar wind model for space weather predictions, *J. Geophys. Res.*, *106*, 20,985.
- Fry, C. D., M. Dryer, C. S. Deehr, W. Sun, S.-I. Akasofu, and Z. Smith (2003), Forecasting solar wind structures and shock arrival times using an ensemble of models, *J. Geophys. Res.*, *108*(A2), 1070, doi:10.1029/2002JA009474.
- Gopalswamy, N. (2004), A global picture of CMEs in the inner heliosphere, in *The Sun and the Heliosphere as an Integrated System*, *Astrophys. Space Sci. Libr. Ser.*, edited by G. Poletto and S. Suess, chap. 8, p. 201, Springer, New York.
- Hakamada, K., and S.-I. Akasofu (1982), Simulation of three-dimensional solar wind disturbances and resulting geomagnetic storms, *Space Sci. Rev.*, *31*, 3.
- Hick, P. P., A. Buffington, and B. V. Jackson (2005), The SMEI real-time data pipeline: From raw CCD frames to photometrically accurate full-sky maps, in *Solar Physics and Space Weather Instrumentation*, *Proc. SPIE Int. Soc. Opt. Eng.*, *5901*, 59011B, doi:10.1117/12.617996.
- Howard, T. A., and S. J. Tappin (2005), Interplanetary shocks unconnected with earthbound coronal mass ejections, *Geophys. Res. Lett.*, *32*, L14106, doi:10.1029/2005GL023056.
- Howard, T. A., D. F. Webb, S. J. Tappin, D. R. Mizuno, and J. C. Johnston (2006), Tracking halo coronal mass ejections from 0–1 AU and space weather forecasting using the Solar Mass Ejection Imager (SMEI), *J. Geophys. Res.*, *111*, A04105, doi:10.1029/2005JA011349.
- Illing, R. M. E., and A. J. Hundhausen (1983), Possible observation of a disconnected magnetic structure in a coronal transient, *J. Geophys. Res.*, *88*, 10,210.
- Jackson, B. V. (1985), Imaging of coronal mass ejections by the Helios spacecraft, *Sol. Phys.*, *100*, 563.

- Jackson, B. V., H. S. Hudson, J. D. Nichols, and R. E. Gold (1989), Design considerations for a 'Solar Mass Ejection Imager' on a rotating spacecraft, in *Solar System Plasma Physics, Geophys. Monogr. Ser.*, vol. 54, edited by J. H. Waite Jr., J. L. Burch, and R. L. Moore, p. 291, AGU, Washington, D. C.
- Jackson, B. V., et al. (2004), The Solar Mass Ejection Imager (SMEI) mission, *Sol. Phys.*, 225, 177–207.
- Jackson, B. V., A. Buffington, P. P. Hick, and Y. Yu (2005), Low-resolution three dimensional reconstruction of CMEs using solar mass ejection imager (SMEI) data, in *Solar Physics and Space Weather Instrumentation, Proc. SPIE Int. Soc. Opt. Eng.*, 5901, 590101, doi:10.1117/12.616329.
- Jackson, B. V., A. Buffington, P. P. Hick, X. Wang, and D. F. Webb (2006), Preliminary analysis of the heliospheric response to the 28 October 2003 CME using SMEI white-light observations, *J. Geophys. Res.*, 111, A04S91, doi:10.1029/2004JA010942.
- Johnston, J. C., D. R. Mizuno, D. F. Webb, T. A. Kuchar, and T. A. Howard (2005), Tracking coronal mass ejections with a heliospheric imager: Case studies from the Solar Mass Ejection Imager, *Eos Trans. AGU*, 86(18), Jt. Assem. Suppl., Abstract SH52A-03.
- Joselyn, J. A. (1995), Geomagnetic activity forecasting: The state of the art, *Rev. Geophys.*, 33(3), 383.
- Kahler, S. W., and G. M. Simnett (2005), Imaging interplanetary disturbances causing forbush decreases, *Proc. Int. Conf. Cosmic Ray 29th*, 2, 267–270.
- Kuchar, T. A., D. R. Mizuno, C. N. Arge, D. F. Webb, S. W. Kahler, and J. C. Johnson (2004), Comet tail disconnections observed by SMEI, *Eos Trans. AGU*, 85(47), Fall Meet. Suppl., Abstract SH21A-0396.
- Leighly, J. B. (1955), Aitoff and Hammer: An attempt at clarification, *Geogr. Rev.*, 45, 246.
- Leinert, C., H. Link, E. Pitz, N. Salm, and D. Knuppelberg (1975), Helios zodiacal light experiment, *Raumfahrtforschung*, 19, 264.
- Manoharan, P. K. (2006), Evolution of coronal mass ejections in the inner heliosphere: A study using white-light and scintillation images, *Solar Phys.*, 235(1–2), 345, doi:10.1007/s11207-006-0100-y.
- McKenna-Lawlor, S., M. Dryer, M. D. Kartalev, Z. Smith, C. D. Fry, W. Sun, C. S. Deehr, K. Kecskemety, and K. Kudela (2006), Real-time predictions of the arrival at the Earth of flare-generated shocks during solar cycle 23, *J. Geophys. Res.*, doi:10.1029/2005JA011162, in press.
- Mizuno, D. R., et al. (2005), Very high altitude aurora observations with the Solar Mass Ejection Imager, *J. Geophys. Res.*, 110, A07230, doi:10.1029/2004JA010689.
- Murtagh, W., et al. (2004), Service assessment, intense space weather storms October 19–November 07, 2003, report, Natl. Oceanic and Atmos. Admin., Natl. Weather Serv., Silver Spring, Md.
- Reiner, M. J., B. V. Jackson, D. F. Webb, D. R. Mizuno, M. L. Kaiser, and J.-L. Bougeret (2005), CME kinematics deduced from white-light (SMEI) and radio (Wind/WAVES) observations, *J. Geophys. Res.*, 110, A09S14, doi:10.1029/2004JA010943.
- Simnett, G. M. (2005), CMES observed by SMEI which are not seen by LASCO, in *Proceedings of Solar Wind 11/SOHO 16, Connecting Sun and Heliosphere*, edited by B. Fleck and T. H. Zurbuchen, *Eur. Space Agency, Spec. Publ.*, SP-592, 767.
- Simnett, G. M., and S. W. Kahler (2005), Interplanetary CMES without observed coronagraph CMES, in *Proc. Int. Conf. Cosmic Ray 29th*, 1, 165–168.
- Simnett, G. M., et al. (1997), Observations of disconnected magnetic structures out to beyond 28 solar radii during coronal mass ejections, *Sol. Phys.*, 175, 685.
- Smith, Z., and M. Dryer (1990), MHD study of temporal and spatial evolution of simulated interplanetary shocks in the ecliptic plane within 1 AU, *Sol. Phys.*, 129, 387.
- Tappin, S. J. (1984), Transient disturbances in the solar wind, Ph.D. thesis, Univ. of Cambridge, Cambridge, UK.
- Tappin, S. J. (2005), The deceleration of an interplanetary transient from the sun to 1 AU, *Sol. Phys.*, 233, 233, doi:10.1007/s11207-006-2065-2.
- Tappin, S. J., et al. (2004), Tracking a major interplanetary disturbance with SMEI, *Geophys. Res. Lett.*, 31, L02802, doi:10.1029/2003GL018766.
- Webb, D., and J. Allen (2004), Spacecraft and ground anomalies related to the October–November 2003 solar activity, *Space Weather*, 2, S03008, doi:10.1029/2004SW000075.
- Webb, D. F., and E. W. Cliver (1995), Evidence for magnetic disconnection of mass ejections in the corona, *J. Geophys. Res.*, 100, 5853–5870.
- Webb, D. F., and R. A. Howard (1994), The solar cycle variation of coronal mass ejections and the solar wind mass flux, *J. Geophys. Res.*, 99, 4201–4220.
- Webb, D. F., and A. J. Hundhausen (1987), Activity associated with the solar origin of coronal mass ejections, *Sol. Phys.*, 108, 383.
- Webb, D. F., and B. V. Jackson (1990), The identification and characteristics of solar mass ejections observed in the heliosphere by the Helios 2 photometers, *J. Geophys. Res.*, 95, 20,641.
- Webb, D. F., J. C. Johnston, and R. C. Radick (2002), The Solar Mass Ejection Imager (SMEI): A new tool for space weather, *Eos Trans. AGU*, 83, 33.
- Webb, D. F., J. Burkepille, T. G. Forbes, and P. Riley (2003), Observational evidence of new current sheets trailing CMES, *J. Geophys. Res.*, 108(A12), 1440, doi:10.1029/2003JA009923.

A. Buffington, P. P. Hick, and B. V. Jackson, CASS, 9500 Gilman Drive, University of California, San Diego, La Jolla, CA 92093-0424, USA.

M. P. Cooke, C. J. Eyles, G. M. Simnett, and S. J. Tappin, School of Physics and Astronomy, University of Birmingham, Birmingham B15 2TT, UK.

C. D. Fry, Exploration Physics International, Inc., Huntsville, AL, USA.
L. C. Gentile, T. A. Kuchar, D. R. Mizuno, and D. F. Webb, Institute for Scientific Research, Boston College, Chestnut Hill, MA, USA. (david.webb.ctr@hanscom.af.mil)

J. G. Hewitt, P. E. Holladay, J. C. Johnston, J. B. Mozer, and S. Price, Air Force Research Laboratory, Space Vehicles Directorate, Hanscom AFB, MA, USA.

T. A. Howard, Physics Department, Montana State University, Bozeman, MT, USA.

R. R. Radick, Air Force Research Laboratory, Space Vehicles Directorate, Sunspot, NM, USA.